sciendo
Austrian Journal of Earth Sciences | Vienna | 2022 | Volume 115 | 15 - 40 | DOI: 10.17738/ajes.2022.0002

Petrological and geochronological investigations on the individual nappes of the Meran-Mauls nappe stack (Austroalpine unit/South Tyrol, Italy)

Hannah Pomella[1]*, Daniel Costantini[2], Paul Aichholzer[1], Martin Reiser[3], Ralf Schuster[3], Peter Tropper[4]

[1)] Institute of Geology, University of Innsbruck, Innrain 52f, 6020 Innsbruck, Austria. Hannah.Pomella@uibk.ac.at, Aichholzer.Paul@gmail.com

[2)] Landesamt für Geologie und Baustoffprüfung, Eggentaler Straße 48 - 39053 Kardaun, Autonomous Province of Bozen, Italy. Daniel.Costantini@provinz.bz.it

[3)] Geologische Bundesanstalt, Neulinggasse 38, 1030 Wien, Austria. Martin.Reiser@geologie.ac.at; Ralf.Schuster@geologie.ac.at

[4)] Institute of Mineralogy and Petrography, University of Innsbruck, Innrain 52f, 6020 Innsbruck, Austria. Peter.Tropper@uibk.ac.at

[*)] Corresponding author, Hannah Pomela

KEYWORDS

Eastern Alps, Austroalpine Unit, Meran-Mauls nappe stack, metamorphic evolution, geochronology

Abstract

The Meran-Mauls nappe stack is part of the Austroalpine unit in South Tyrol (Italy). There it holds a special position directly in front of the Southalpine Dolomites indenter and west of the Tauern Window. It is situated in the hanging wall of the Southalpine unit, above a NW dipping segment of the Periadriatic fault system, namely the Meran-Mauls fault. Also all other sides are defined by Oligocene-Miocene strike-slip and normal faults. Based on recent mapping the Meran-Mauls nappe stack consists of three nappes separated by NW to NNW dipping shear zones. The lowermost nappe in the southwest is represented by the Schenna (Scena) unit. It is overlain along the Masul shear zone by a nappe consisting of the Hirzer (Punta Cervina) unit and the Pens (Pennes) unit including Triassic (meta)sediments. Separated by the Fartleis fault the St. Leonhard (San Leonardo) unit forms the uppermost nappe. The aim of this study is to describe the individual units and the separating structural elements more properly, based on new structural, petrological, geothermobarometric and geochronological data and to compare these units to other Austroalpine elements in the vicinity. Sillimanite-bearing paragneiss, minor amphibolite and quartzite as well as a distinct marble layer close to its base characterise the Schenna unit. Further, it contains pegmatite dikes, presumably Permian in age. Amphibolite-facies P-T conditions of c. 0.55 ± 0.15 GPa and 600 ± 100°C are thus correlated with a Permian metamorphic imprint. The Masul shear zone mostly consists of mylonitic paragneiss of the Hirzer unit. It is pre-Alpine in age and probably formed during the Jurassic. For the paragneiss of the Hirzer unit upper greenschist- to amphibolite-facies metamorphic conditions of 0.4-0.50 ± 0.15 GPa and 550 ± 70°C are attributed to the Variscan tectonometamorphic imprint. The whole Pens unit represents a shear zone. Due to the occurrence of Permotriassic (meta)-sediments within this shear zone, it is an Alpine structure, as well as the bordering Fartleis fault. Rb/Sr biotite ages yield sometimes partly reset pre-Alpine age values in the whole Meran-Mauls nappe stack, indicating a pervasive anchizonal to lowermost greenschist-facies metamorphic overprint during the Eoalpine tectonometamorphic event. Tectonostratigraphically the Meran-Mauls nappe stack can be attributed to the Drauzug-Gurktal nappe system. The latter forms the uppermost structural element of the Austroalpine nappe stack and thus only shows a weak Eoalpine metamorphic overprint. With respect to its special lithologic composition the Schenna unit can be correlated with the Tonale unit in the southwest and the Strieden-Komplex in the east.

1. Introduction

Between Meran and Mauls in South Tyrol (Italy) the Austroalpine unit in front of the edge of the Dolomites indenter (Frisch et al., 2000) (Fig. 1) is comprised of a stack of nappes predominantly built up by metamorphic basement rocks (Bargossi et al., 2010) with minor remnants of a Triassic cover sequence (Furlani, 1921) preserved along an internal nappe boundary (Fig. 2). The Austroalpine unit is separated from the Southalpine unit along the NW-NNW dipping Meran-Mauls fault (MMF), which represents a segment of the Periadriatic fault system (Fig. 1 and Fig. 2). In older maps and publications the Austroalpine nappe stack in the hanging wall of the MMF was part of the so called "Meran-Mauls-Antholz Complex" (Sander and Hammer, 1926) or later the "Meran-Mauls Basement" (Baggio et al., 1971; Del Moro et al., 1982; Spiess, 1995). The latter term was used to summarise the entire polymetamorphic Austroalpine basement units between the base of the Schneeberg unit

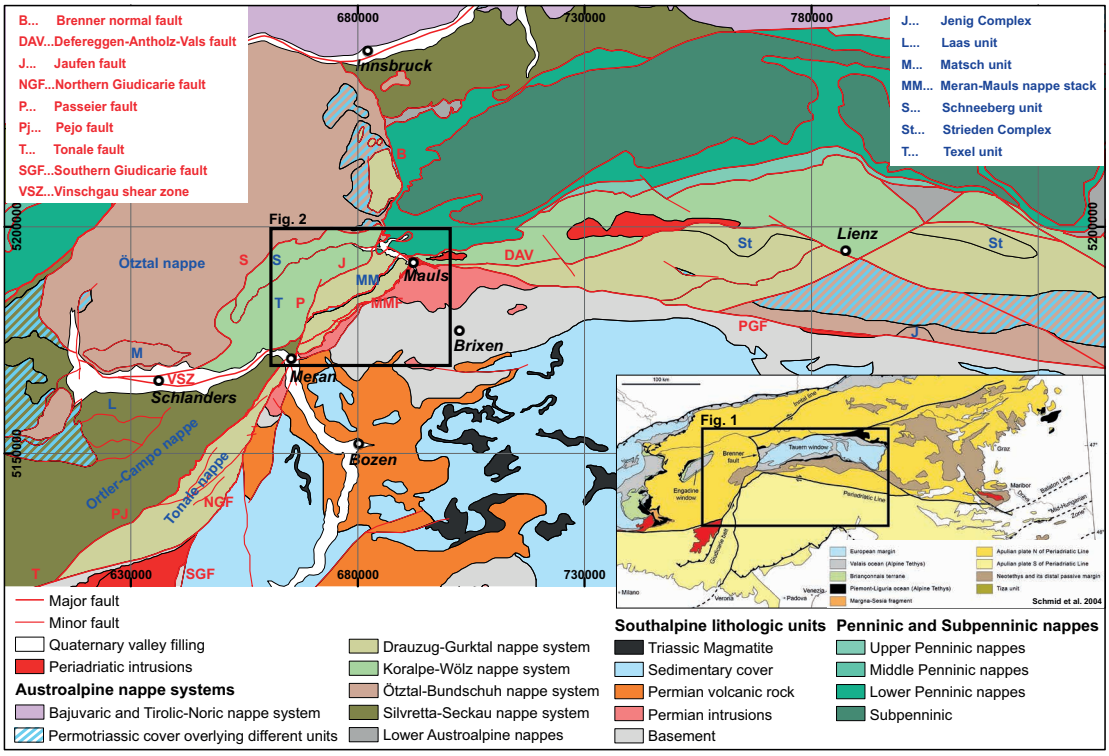

Figure 1: Tectonic overview map compiled from Pomella et al. (2016), Schmid et al. (2004), Autonomous Province Bozen-Bolzano Geo-Browser (Tectonic overview and CARG maps; https://maps.civis.bz.it/?context=PROV-BZ-GEOLOGY-CARG), Ralf Schuster (personal communication).

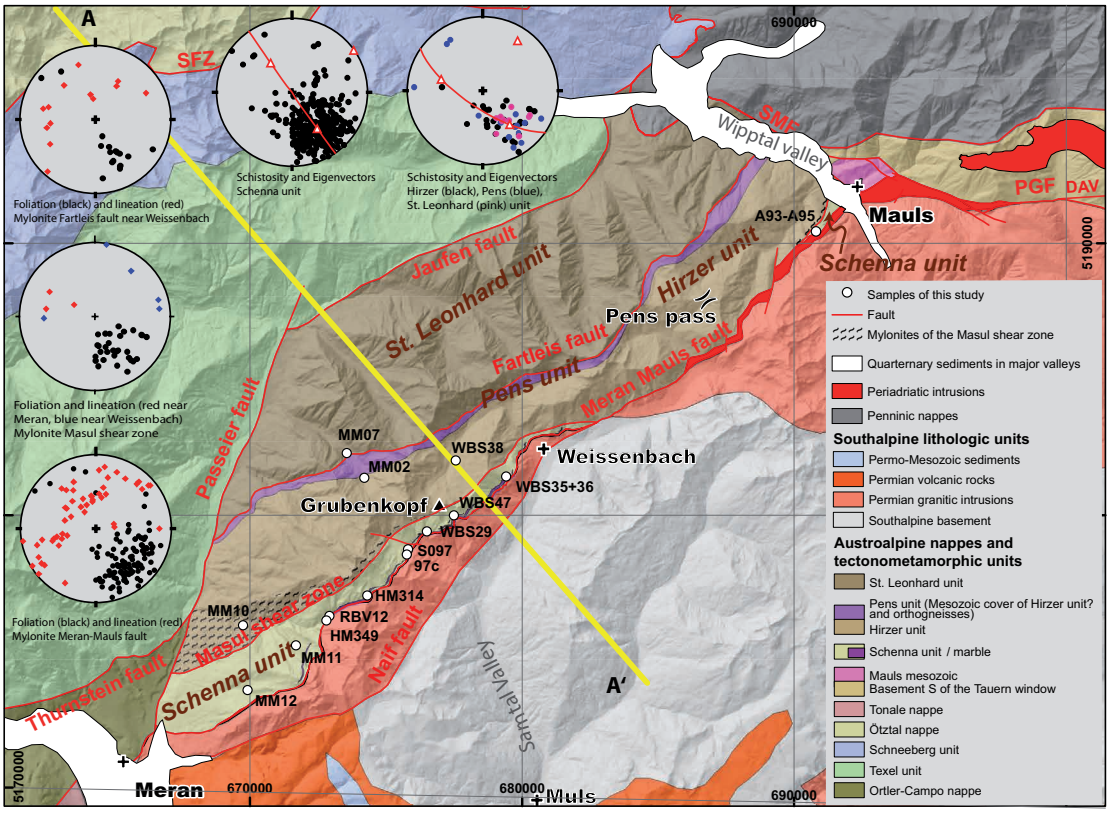

Figure 2: Tectonic map of the research area modified after Pomella et al. (2016) and CARG Foglio 013 Meran/Merano (AA.VV., 2010). The stereoplots indicate the orientation of the schistosity of the different units as well as the orientation of foliation and stretching lineation measured in mylonites of the Meran Mauls fault (MMF), the Masul shear zone and the Fartleis fault. The structural data are presented in chapter "4.1 Structural field data" and discussed in section "5.3 Formation of the Meran-Mauls nappe stack". The white dots mark the sample locations; the corresponding coordinates are given in Appendix Table A2. SFZ: Schneeberg fault zone. DAV: Defereggen-Antholz-Vals fault; PGF: Pustertal-Gailtal fault; SMF: Sprechenstein-Mauls fault.

in the northwest, characterised by a pressure-dominated Eoalpine metamorphic imprint only, and the Meran-Mauls fault (MMF) in the southeast (Fig. 2). According to this definition, the Meran-Mauls Basement includes an Eoalpine (Cretaceous) amphibolite- to eclogite-facies metamorphic part in the northwest (now named the Texel unit) and an Eoalpine anchizonal to lowermost greenschist-facies metamorphic part in the southeast. In the southeastern part, the Eoalpine metamorphism was not strong enough to completely reset the pre-Alpine Rb/Sr biotite ages (Baggio et al., 1971; Del Moro et al., 1982). These two parts are separated by the Passeier-Jaufen fault system. More recent publications (e.g. Sölva et al., 2001; Tropper and Recheis, 2003; Schmid et al., 2004; Pomella et al., 2012) restrict the Meran-Mauls Basement to the Eoalpine weakly metamorphic units to the southeast of the Passeier-Jaufen fault system. In the map of the Italian CARG project 013 – Meran/Merano (AA.VV., 2010; https://www.isprambiente.gov.it/Media/carg/13_MERANO/Foglio.html) the term Meran-Mauls Basement is no longer used and the area between the Passeier-Jaufen fault system and the MMF is subdivided into four tectonic units separated by important NW to NNW dipping shear zones and faults respectively. We support the elimination of the term "Meran-Mauls Basement", as this designation does not take into account the remnants of the Triassic cover and the term is used in older literature inconsistently. When referring not to the single units but to the entire nappe stack between the Passeier-Jaufen fault system and the MMF we suggest using the term "Meran-Mauls nappe stack" (MMNS). According to Schmid et al. (2004) this nappe stack is part of the Drauzug-Gurktal nappe system, forming the structural uppermost element of the Austroalpine unit.

Several authors published thermochronological data for the MMNS, concentrating along tectonic borders and internal faults in the northeastern part of the unit (chapter 4.1). Rb/Sr as well as K/Ar ages on biotite and white mica range from 140 to 326 Ma (Satir, 1975; Del Moro et al., 1982; Thöni, 1983; Spiess, 1995). They indicate a pre-Alpine age of the main metamorphic imprint of the individual nappes. During the Eoalpine metamorphic overprint, temperatures did not exceed about 350°C because the Rb/Sr and K/Ar systems in both micas was not reset completely. Younger ages in the range of 140-250 Ma were measured close to the Passeier-Jaufen fault system and interpreted by Spiess (1995) as Variscan cooling ages partly reset during the Eoalpine overprint. In contrast, Schuster et al. (2001) speculated about the influence of a Permian high-temperature/low-pressure (HT/LP) event to explain the age values in the range of 250-270 Ma. This speculation was triggered by the occurrence of pegmatite dikes within sillimanite-bearing paragneiss in the southernmost part of the MMNS, which are thought to be Permian in age. However, from this part of the MMNS, which is nowadays defined as the Schenna unit no geochronological ages were available.

The new subdivision of the MMNS demands for a better characterisation and definition of the individual nappes and their bounding structures. However, the necessary structural, petrological, geothermobarometric and geochronological data are only partly available. For example, the Schenna unit is peculiar because of the presence of pegmatitic dikes and statically growing sillimanite in hosting paragneiss (Fig. 3), but the PT conditions as well as the timing of sillimanite formation and pegmatite emplacement is still not constrained. In this investigation we performed fieldwork and petrological, geochemical and Rb/Sr isotopic investigations in order to more properly characterize the individual units of the MMNS in terms of lithologies and metamorphic evolution. Special focus was given to the sillimanite-bearing paragneiss and marble of the Schenna unit. In addition, Rb/Sr biotite ages were measured from all nappes in the southwestern part of the MMNS where these data were missing.

2. Geological setting

The MMNS holds a very special position within the Austroalpine unit. It is situated along the southern margin towards the Southalpine unit, directly in front of the edge of the Dolomites indenter (Frisch et al., 2000). This indenter was also crucial for the exhumation of the Subpenninic and Penninic units within the Tauern Window, which borders the MMNS in the northeast (e.g. Favaro et al., 2017; Reiter et al., 2018). Indentation in late Oligocene-Miocene times caused yet another disruption of the prior existing complex nappe stack and fault pattern of the area (e.g. Pomella et al., 2011; Klotz et al., 2019). The MMNS is bordered by the Passeier fault in the WNW, the Jaufen fault in the NNW, and the MMF in the SE (Fig. 2). Towards ENE the nappe stack ends in the Wipptal valley (Alta Vall'Isarco) and is probably cut off by a fault related to the Sprechenstein-Mauls fault system (Brandner et al., 2008; Bistacchi et al., 2010; Schiavo et al., 2015). Internally it can be subdivided in four (AA.VV., 2010; Bargossi et al., 2010) or three (Pomella et al., 2012) tectonic units respectively: From south (bottom) to north (top) the units are named Schenna (Scena), Hirzer (Punta Cervina), Pens (Pennes), and St. Leonhard (San Leonardo) unit and are separated by the Masul shear zone and the Fartleis fault (Pennes-Mules shear zone) respectively. In the following section the lithological units of the Meran-Mauls nappe stack are briefly characterised. Detailed petrographic and structural descriptions are available in the explanatory notes of the map 013 – Meran/Merano (Bargossi et al., 2010).

The **Schenna (Scena) unit** forms the hanging wall of the MMF on top of the Southalpine unit from Meran in the southwest, up to Weissenbach in the Sarntal valley where it wedges out between the MMF and the Masul shear zone. According to detailed mapping in the course of the present study, it reoccurs further to the NE as a thin slice in the hanging wall of the MMF (Fig. 2). The Schenna unit consists predominantly of kyanite- and sillimanite-

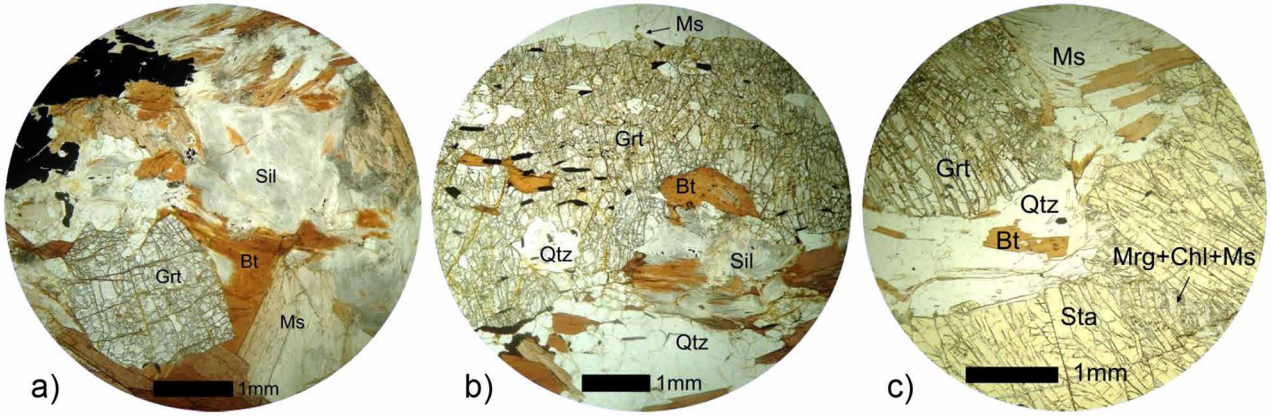

Figure 3: Thin section photos (parallel nicols) of paragneiss belonging to the Schenna unit. (a) Typical mineral assemblage: fibrolitic sillimanite (Sil), garnet (Grt), biotite (Bt), muscovite (Ms), quartz (Qtz), plagioclase (Pl), and opaque minerals (sample MM12); (b) pseudomorphic replacement of garnet by fibrolitic sillimanite and biotite (sample MM12); (c) staurolite (Sta) bearing paragneiss. Staurolite is replaced by margarite (Mgr), chlorite (Chl), and muscovite (Ms) (sample RBV12).

bearing paragneiss and micaschist, subordinately amphibolite, marble, calcsilicate schist, and quartzite appear. The calcite and/or dolomite marble forms a more or less continuous, up to 20 m thick layer occurring parallel and close to the MMF between Meran and Weissenbach (Fig. 2). This layer was already described by Sander (1906). Additionally, discordant pegmatite dikes and bodies occur, which were mined in the Masul valley for muscovite and later on also beryl from approximately 1930 to 1950 (Exel, 1998). To the north, the Schenna unit is bordered by the Masul shear zone.

The **Hirzer (Punta Cervina) unit** comprises kyanite-bearing paragneiss, micaschist, orthogneiss as well as subordinate amphibolite and quartzite. Most of the mylonites of the Masul shear zone developed from para- and orthogneiss of the Hirzer unit. The shear zone reaches several 100 m of thickness on its western end and thins out towards NE until it is cut off by the MMF (Fig. 2). The mylonites show an upper greenschist-facies overprint (Bistacchi et al., 2008) with biotite often stable along the NW-NNW (320-340°/45-55°) dipping foliation. The stretching lineation dips towards WNW-NW (280-320°), asymmetric porphyroclasts and S-C shear bands suggest reverse SE-directed motions. Cataclastic overprint of the mylonitic fabrics is confined within discrete fault zones (Bistacchi et al., 2008).

The overlying **Pens (Pennes) unit** comprises a crystalline basement, predominantly composed of leucocgranitic orthogneiss, and an up to 150 m thick Triassic cover sequence. There is still a debate whether the contact to the underlying Hirzer unit is of tectonic or stratigraphic nature. Pomella et al. (2012) interpreted the sedimentary succession described above as the (para-)autochthonous Mesozoic cover of the Hirzer unit, however it might also represent an independent tectonic unit. In any case, the entire unit is deformed and boudinaged and Bargossi et al. (2010) described it therefore as a NW dipping, transpressive shear zone named the Pennes-Mules shear zone. The eastern part of the Pens unit is dominated by the Triassic sedimentary succession which comprises stacked and folded slices of conglomerate, dolomite and often fossil-bearing limestone showing only a weak (anchizonal to lowermost greenschist-facies) metamorphic overprint. In the literature this succession is also known as the "Pens Triassic" (Furlani, 1921) or "Stilfes Triassic" (Schindelmayr, 1968) and interpreted as the lateral equivalent to the "Mauls Triassic" (Brandner et al., 2008; Schiavo et al., 2015) occurring further to the east. Towards the west, the sedimentary succession thins out and the mylonitic leucogranitic orthogneiss (Bistacchi et al., 2008; Bargossi et al., 2010) dominates the Pens unit. The top of the Pens unit is bordered by a brittle fault zone known as Fartleis fault (Furlani, 1921; Spiess, 1992; Pomella et al., 2012) and overthrust by the St. Leonhard unit, first under ductile and finally under brittle conditions.

The **St. Leonhard (San Leonardo) unit** consists mostly of banded paragneiss with porphyroclasts of garnet, staurolite and kyanite. Orthogneiss is also common and quartzite, amphibolite and micaschist occur subordinately.

The MMF borders the MMNS towards the Southalpine unit in the SE. All along the MMF and its southwestern continuation represented by the Giudicarie fault system slices of tonalite and carbonate sequences occur. Typically, they show cataclastic or mylonitic fabrics. The tonalite bodies belong to the Periadriatic intrusions and are Oligocene in age (Pomella et al., 2011). The carbonate-rich sequences include predominantly yellowish limestone (Prosser, 2000; Viola et al., 2001), nearly undeformed dolomite, phyllite with rounded quartz pebbles, as well as rauhwacke. Pomella (2010) interpreted these slices as remnants of Permotriassic cover sequences of the Austroalpine unit based on their weak metamorphic overprint and tectonic position.

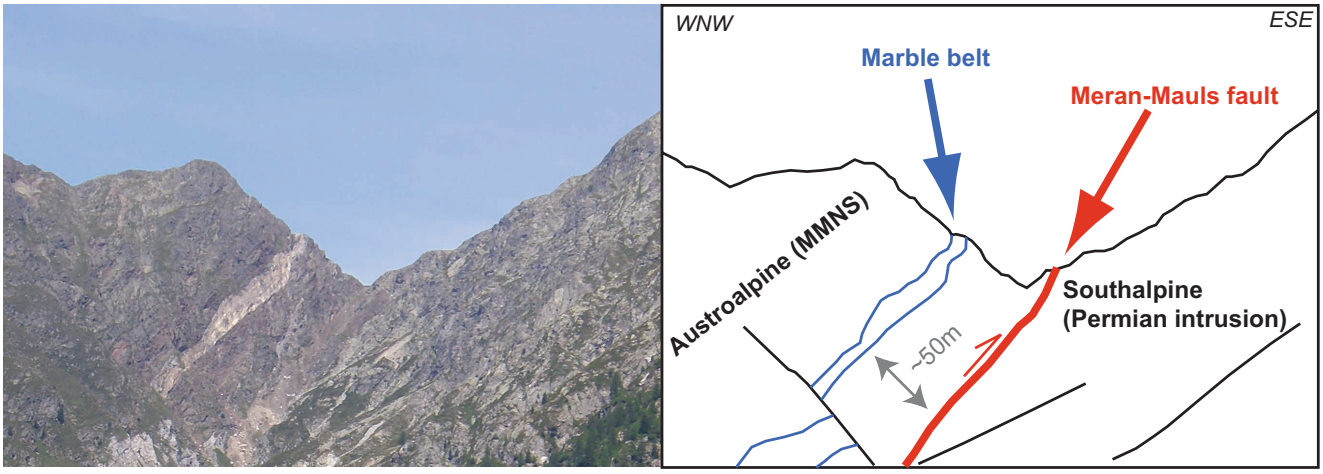

Figure 4: The Meran-Mauls fault in the Rötenbach valley NE of Meran seen from SSW. The Ifinger granodiorite in the right part of the photo is overthrust by paragneiss of the Schenna unit. Within the paragneiss, an intensively deformed marble layer occurs in the vicinity of the fault.

3. Analytical methods

3.1 Mineral chemistry

Chemical compositions of minerals were analysed using a JEOL 8100 SUPERPROBE electron probe micro analyser (EPMA) at the Institute of Mineralogy and Petrography of the University of Innsbruck. Analytical conditions were 15 kV acceleration voltage and 10 nA beam current. The following mineral standards were used for calibration: quartz (Si), diopside (Ca, Mg), orthoclase (K), almandine (Fe), jadeite (Na), corundum (Al), chromite (Cr), rutile (Ti) and rhodonite (Mn). The counting times were 20 s for the peak and 10 s for the background. The data analysed using an open beam (3x3 µm) to prevent volatilization of alkalis.

3.2 Rock chemistry

Geochemical analyses on marble samples were carried out using an energy dispersive X-ray fluorescence analyzer (EDXRFA) Spectro-Xepos at the Institute of Mineralogy and Petrography of the University of Innsbruck. Results are given in Appendix Table A1.

3.3 Sr-isotopic analyses on marble and Rb/Sr dating

For Sr-isotope analyses of marble about 70 mg of whole-rock powder were dissolved in 0.1 n HCl and the undissolved part of the sample was extracted by a centrifuge immediately after dissolution of the carbonate.

For Rb/Sr geochronology biotite was separated by the standard methods of crushing, grinding, sieving and magnetic separation. Samples used for dissolution weighed about 100 mg for whole rock powder and 200 mg for biotite. The chemical preparation was performed at the Geological Survey of Austria in Vienna, following the procedure described by Sölva et al. (2005). Isotopic measurements were carried out at the Department of Geological Sciences at the University of Vienna using a ThermoFinnigan® Triton TI TIMS. Sr was run from Re double filaments, whereas Rb was evaporated from a Ta single filament. The NBS987 standard yielded $^{87}Sr/^{86}Sr$ = 0.710255±4 (n=5) during the period of measurements. Calculation of ages was done using Isoplot software Version 4.16 (Ludwig, 2008) assuming an uncertainty of 1% on the $^{87}Rb/^{86}Sr$ ratios. Uncertainties on the $^{87}Sr/^{86}Sr$ isotope ratios are quoted as 2σ. Biotite ages were calculated using the Rb-decay constant of 1.42 ± $0.004\times10^{-11}year^{-1}$. All uncertainties and final ages are quoted at the 2σ level.

4. Results

Locations for all samples referred in this chapter are shown in Figure 1 and coordinates given in Appendix Table A2.

4.1 Structural field data

The structural field data in Figure 2 are reported in order to give an overview on the orientation of the schistosity in the individual units and the kinematics of the major faults. Over the entire MMNS the orientation of the schistosity is constantly dipping towards NW with 40-70° and the fold axes are shallowly dipping towards NE-NNE, based on a calculation via Eigenvector analysis (software Tectonics FP; Reiter and Acs, 1996-2000; Ortner et al., 2002). The foliation along the MMF is variable ranging from N to W dipping. No spatial trend in the orientation could be identified and the observed variation is probably only due to boudinage of tonalite bodies and the marble layer of the Schenna unit present along the fault (e.g. Fig. 4). The orientation of the stretching lineation observed in the Austroalpine basement shows two clusters. The older horizontal stretching lineation indicates a dextral sense of shear. The overprinting down-dip lineation indicates top-SE thrusting. Therefore, the MMF represents a dextral strike slip fault reactivated as a top-SE thrust fault (see also Pomella et al., 2011). The marble layer is highly deformed and shows a penetrative mylonitic foliation (Fig. 5a) dipping towards NW and a distinct dip-slip stretching lineation only. Sigma clasts in thin sections indicate top-to-SE reverse faulting (Figs 5e + f). The

whole layer appears boudinaged as its thickness is highly variable also in outcrop scale (Fig. 4).

The mylonitic foliation of the Masul shear zone is strictly dipping towards NNW. Two clusters of lineation can be separated in the plots (Fig. 2), but in this case a clear spatial distribution can be observed: shallow NE dipping strike slip lineations are restricted to outcrops close to the intersection of the Masul shear zone with the MMF near the village of Weissenbach (Rio Bianco). For this group no shear sense could be identified in the field. In contrary, in the southwestern part of the fault zone only steeper WNW dipping lineation with clear top-to-SE reverse shear sense indicators were observed. Structural data of the Fartleis fault presented here were collected only in the area NW and N of Weissenbach. The foliation of the Fartleis fault is NNW dipping. The distribution of lineation shows no cluster but more a girdle distribution. This is in agreement with observations by Bargossi et al. (2010) describing the occurrence of stretching lineation with variable orientation from down-dip to oblique along the westernmost section of the Fartleis fault.

4.2 Petrological and chemical data

In this section the lithologies of the Schenna unit and Hirzer unit are described based on field observations and thin section petrography. Further mineral chemical data on key-lithologies used for geothermobarometric investigations are reported and representative analyses are given in Appendix Table A3 (silicates) and A4 (carbonates).

4.2.1 Schenna unit

Sillimanite-bearing paragneiss with the mineral assemblage of plagioclase + biotite + muscovite + sillimanite + quartz ± kyanite ± garnet ± staurolite ± chlorite ± ilmenite is the dominant lithology. Sillimanite always occurs as fibrolite growing on biotite in the vicinity of garnet (Figs 3a + b). In the southwestern part of the Schenna unit sillimanite aggregates are often visible macroscopically, whereas towards the northeast the aggregates get smaller and are detectably only in thin sections. Garnet is often replaced by biotite along the rims. Staurolite shows pseudomorphic replacement by fine-grained aggregates, which consist of the sheet silicate assemblage muscovite + margarite + chlorite (Fig. 3c). Staurolite occurs as Fe-staurolite with low X_{Mg} [Mg/Mg+Fe)] between 0.11 and 0.17. The Zn contents vary from 0.01 wt.% up to 4 wt.% ZnO. Biotite shows X_{Mg} between 0.44 and 0.5 and Ti-substitution ranges from 0.12 to 0.15 atoms per formula unit (apfu). Muscovite contains a low paragonite (X_{Na}) component [Na/(K+Na+Ca)]<0.14. Margarite is a ternary solid solution between margarite-paragonite-muscovite and shows a strong variation with X_{Ca} [Ca/(Ca+Na+K)] between 0.56 and 0.63. Garnet is almandine-rich ($Alm_{70-73}Prp_{9-12}Sps_{10-12}Grs_{<6}$) and shows no compositional zoning. Plagioclase is present as texturally older and younger grains, with anorthite [X_{An} = Ca/(Ca+Na)] components of >0.30 and <0.10 (albite) respectively. Chlorite is Fe-rich and shows X_{Fe} [Fe/(Fe+Mg)] between 0.58 and 0.63.

Micaschist and garnet micaschist occurs locally intercalated within paragneiss as lenses of a few meters in size. In general, the mineral assemblage is the same as for the paragneiss described above, but it is characterised by a low plagioclase and higher mica content. Close to the MMF the replacement of biotite by chlorite and muscovite indicates a lower greenschist-facies retrograde overprint. Previous authors (Sander and Hammer, 1926; Sander, 1929) mapped these retrograde and deformed lithologies as "phyllonites".

Amphibolite is present only in the structurally lower part of the unit in the vicinity of the MMF. The mineral assemblage of the dark-green coloured rock consists of amphibole + plagioclase + clinozoisite + titanite ± quartz ± biotite ± garnet ± epidote ± chlorite. In thin section the amphibole crystals show no optical zonation. Plagioclase is mostly replaced by zoisite + albite during saussuritisation. Typically, this lithology is massive and shows a fine layering formed by variable contents of amphibole and plagioclase. Locally cm-thick plagioclase-rich layers occur, resulting in a banded appearance. A thin section prepared from a sample taken from the direct contact between amphibolite and marble revealed zoisite with a dark rim of garnet (Fig. 6).

Marble forms a distinct layer intercalated with paragneiss and often associated with quartzite and amphibolite. Within the marble layer macroscopically different types of marble occur. The most important marble varieties are shown in Fig. 5b and listed here. The dominating variety is a fine-grained, grey calcite marble intercalated with calcsilicate layers. The mineral assemblage of this lithology is highly variable (Figs 5a, 5b HM314, and Fig. 7) and includes calcite and/or dolomite + quartz ± plagioclase ± chlorite ± white mica ± rutile ± hematite and occasionally ± phlogopite ± amphibole ± pyroxene ± zoisite (with a rim of garnet; Fig. 6) ± tremolite (up to several cm long crystals). Calcite usually shows high Ca-contents X_{Ca} [Ca/(Ca+Mg+Fe)] ranging from 0.91 to 0.98. White marble as shown in Figure 5b (S097) is also quite common. Typically, it shows a strong mylonitic foliation and a very pronounced dip-slip stretching lineation. The few quartz grains present are very useful for shear sense analyses. A yellowish-brownish, coarse-grained dolomite marble occurs only in a few locations. It shows 1-2 mm sized grains mostly with 120° triple junctions, sometimes beginning dynamic recrystallisation can be observed along grain boundaries. Based on the powder XRD analyses the mineral assemblage consists of 90-95% dolomite and 10-5% calcite + chlorite (Fig. 5b HM349, 5c). In order to study the lateral continuity of the different marble varieties and to reveal a possible stratigraphic succession three parallel sections across the marble layer (Fig. 8) were mapped in detail within erosion channels in the Grubenkar, east of Schafberg peak (Monte delle Pecore). These sections are in a distance of a few hundred meters. Even if there are differences between the sections, fine-grained, white

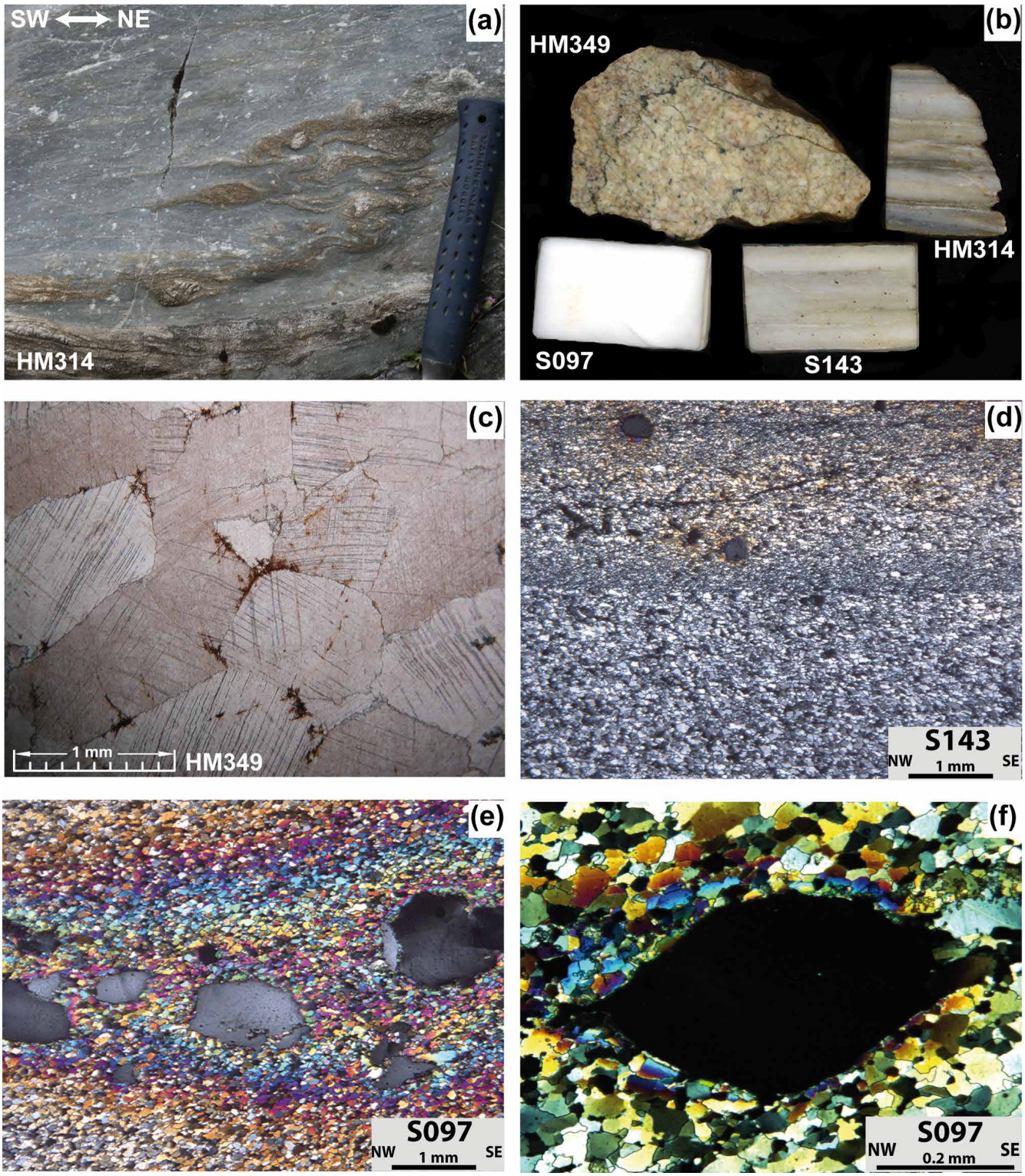

Figure 5: Different types of marble present in the marble belt. Photo (a) shows an intensively folded and sheared marble with siliciclastic layers occurring in the valley Rötenbach, NE of Meran. The surface displayed is oblique to the stretching lineation, therefore the photo should not be used for interpreting shear senses. (b) Samples used for stable isotope, geochemical and Sr-isotopic analyses. Sample HM314 shows the most common type observed. Very pure marble, such as represented by sample S097, occur quite commonly as well. The coarse grained dolomite-marble (HM349) occurs only in a few locations. The huge differences in grain size are depicted in photo (c) (parallel nicols) and (d) (ultra-thin section, crossed nicols). While the coarse grained marble lacks a visible foliation, it is well developed in the fine-grained variety. Photo (e) and (f) were taken from an ultra-thin section (crossed nicols) of a mylonitic marble and show sheared quartz clasts indicating top to SE shearing.

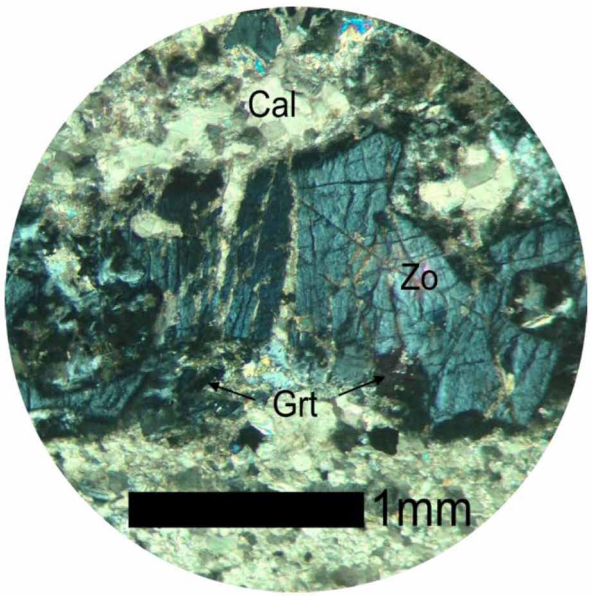

Figure 6: Zoisite (Zo) with a rim of garnet (Grt) surrounded by calcite (sample WBS12).

and greyish calcitic and dolomitic marble is frequent in the lower part of the sections, whereas coarse-grained, yellowish to brownish marble with phlogopite appears in the uppermost part. In two samples (WBS35 and WBS36) compositional zoning of calcite was observed (Fig 9). The cores show Mg contents of 0.02 – 0.04 apfu Mg whereas the rims contain <0.02 apfu Mg. Dolomite also shows chemical zoning with lower Mg contents in the cores ranging from 0.89 to 0.96 apfu Mg while the rims contain 0.92 to 0.99 apfu Mg.

Two samples (WBS35 and WBS47) contain a highly unusual mineral assemblage consisting of calcite + muscovite + kinoshitalite [$Ba(Mg)_3(Al_2Si_2)O_{10}(OH,F)_2$] + apatite + tremolite + titanite + rutile + baotite [$Ba_4(Ti,Nb)_8Si_4O_{28}Cl$] + baricalcite [$BaCa(CO_3)_2$] + pyrite + sphalerite + galena (Degenfelder et al., 2016). Kinoshitalite electron microprobe analysis yielded complete solid solution from phlogopite to kinoshitalite [$Ba(Mg)_3(Al_2Si_2)O_{10}(OH,F)_2$] along the substitution $BaAlK_{-1}Si_{-1}$. Exceptional high F contents of up to 5 wt.% occur in some kinoshitalites and hence some of the analyses can be named fluorokinoshitalite (Degenfelder et al., 2016).

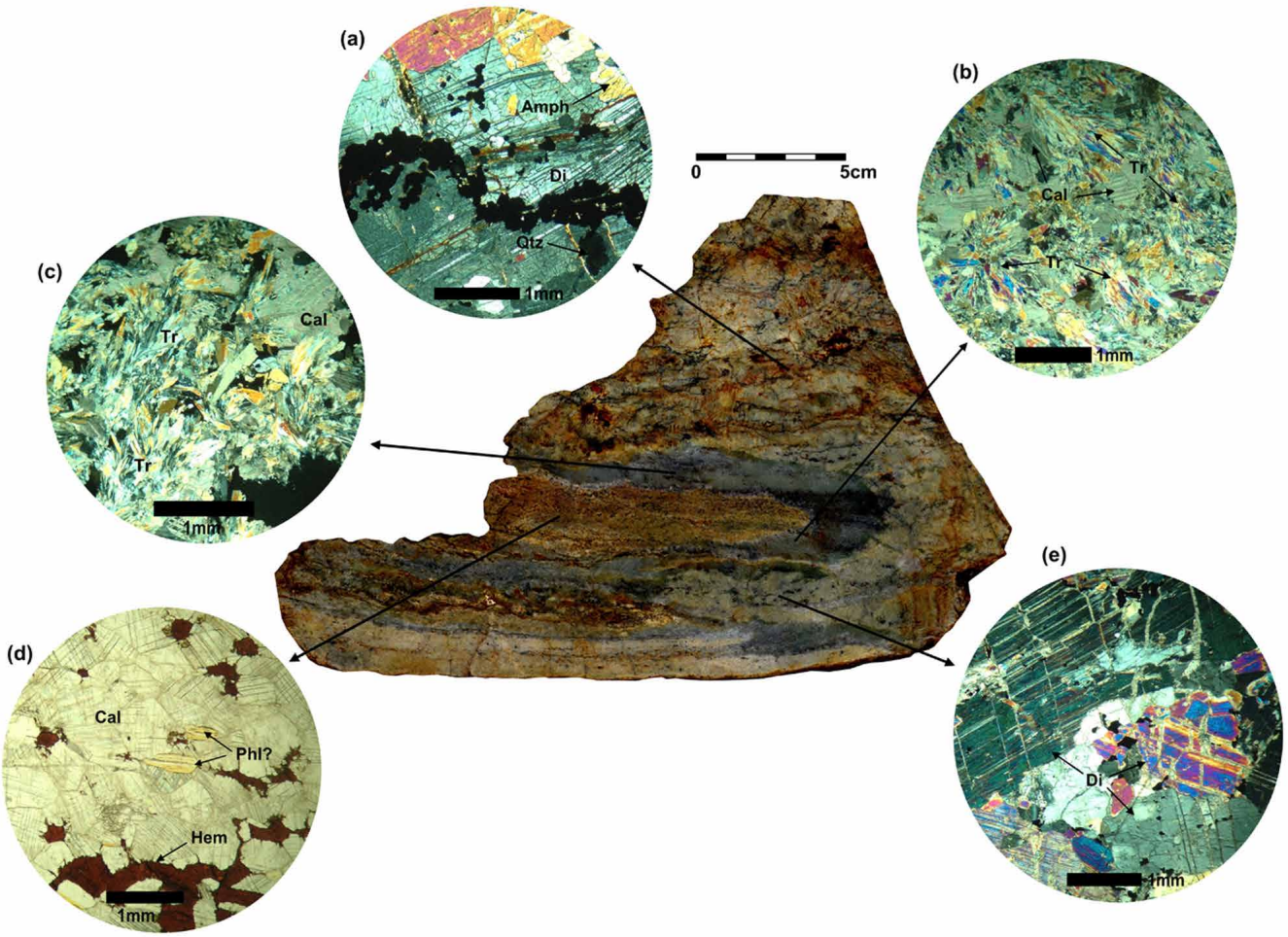

Figure 7: Folded calcsilicate marble boudin near Weissenbach, in the valley Sarntal. The sample WBS36 was examined in different thin-sections according to their mineral properties. (a) Diopside (Di), amphibole (Amph), quartz (Qtz) as well as abundant Fe-oxides; (b) and (c) fascicular, fibrous tremolite accumulations; (d) Calcite-Matrix (Cal) with hematite (Hem) and phlogopite? (Phl); (e) Predominantly clinopyroxene (Cpx) in the form of Diopside (Di).

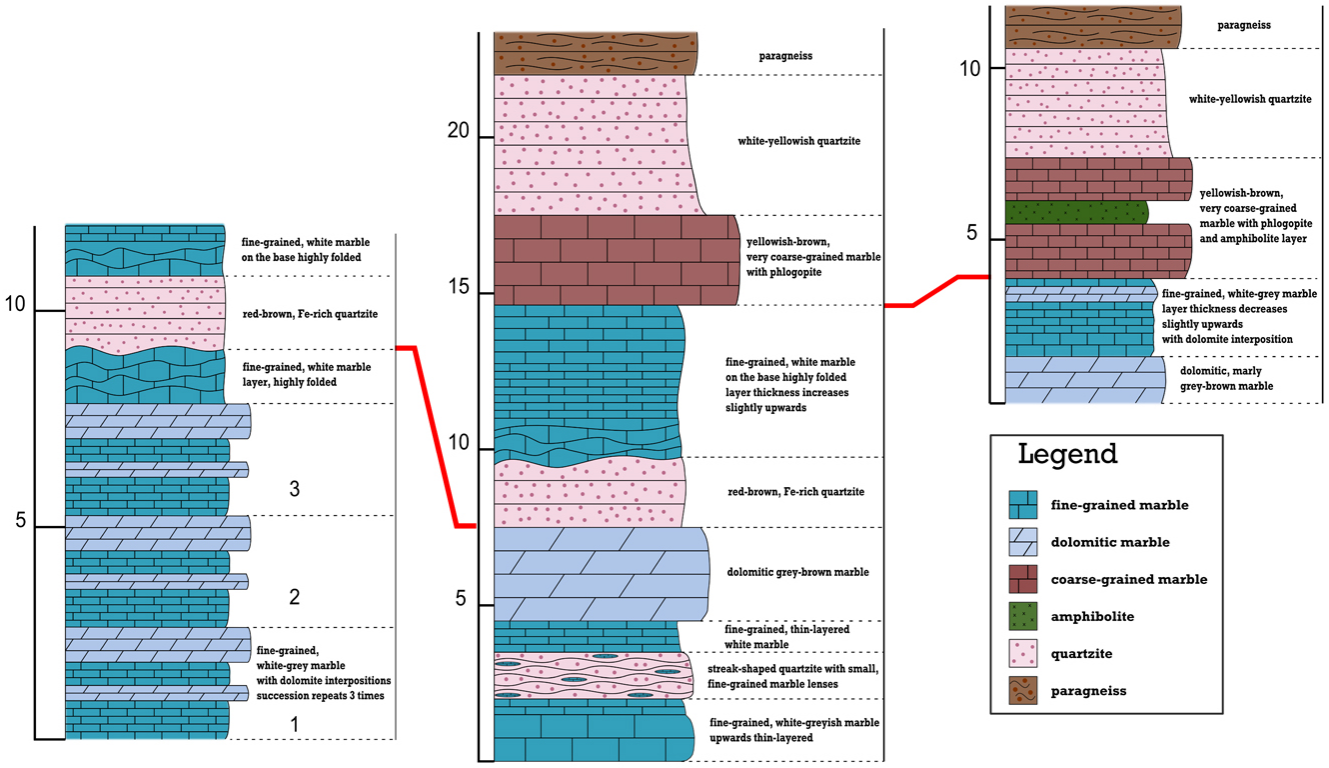

Figure 8: In the Grubenkar, east of the Schafberg peak (Monte delle Pecore), stratigraphic sections can be mapped in several erosion channels. An attempt was made to create a correlation between the different sections (red lines). At the same location sample WBS47 was collected (see Fig. 2 and Appendix Tab. A2 for location)

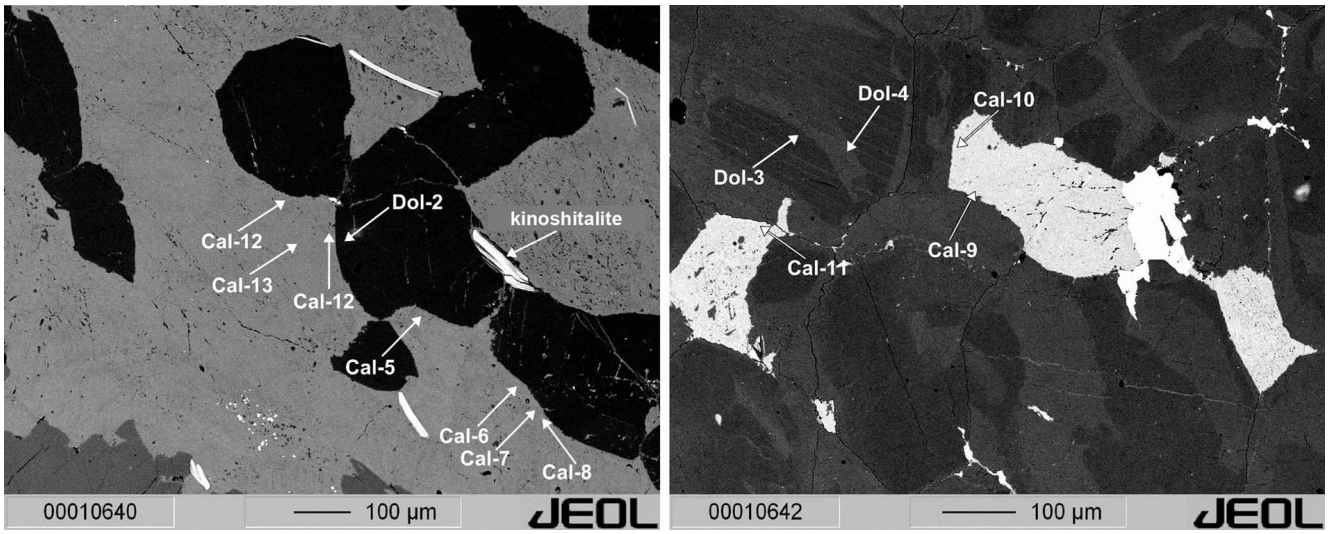

Figure 9: BSE-image of the marble sample WBS35 (left) and of the calcsilicate marble WBS36 (right). The crystals show a clear core- and rim-zoning. The labeling Cal-X (calcite) and Dol-X (dolomite) refer to the analysis compiled in Appendix Table A4, the arrows indicate the position of the measurement.

Quartzite is present as intercalations within and as a layer at the top of the marble succession. It shows a yellow-greyish colour and an assemblage of quartz + (altered) plagioclase + muscovite + chlorite ± biotite ± garnet ± epidote ± apatite ± zircon ± titanite.

Pegmatite lenses are mostly a few meters wide and show the mineral association quartz + K-feldspar + muscovite + plagioclase + tourmaline + garnet ± beryl ± biotite whereby muscovite and beryl crystals can reach a size of up to few decimetres (Baumgarten et al., 1998). Macroscopically they seem undeformed, but in thin sections quartz crystals show undulose extinction and bulging along the grain boundaries indicating dynamic recrystallisation at low temperatures (Stipp et al., 2002). Plagioclase shows deformation lamellae.

4.2.2 Hirzer unit

Paragneiss is the dominant lithology within the Hirzer unit and shows the mineral assemblage of plagioclase + biotite + muscovite + quartz ± kyanite ± garnet ± staurolite ± chlorite ± ilmenite ± graphite and accessory rutile, apatite, and tourmaline. Compared to the Schenna unit the garnet crystals are smaller. Kyanite crystals up to a size of 30 mm can be observed in the Pens pass area growing on the foliation plane with no preferred orientation. In the field it is often difficult to clearly separate **micaschist** from paragneiss as the mineral assemblage is more or less the same with plagioclase + biotite + muscovite + quartz ± kyanite ± garnet ± chlorite ± ilmenite ± graphite, but the paragneiss is coarse-grained with large feldspar porphyroclasts up to several mm in size and smaller quartz grains within the main mica layering.

Amphibolite occurs in up to several hundred-meter-wide lenses e.g. in the area of Weissenbach/Rio Bianco along the summit of Mudatsch/Monte Mudaccio. The mineral assemblage of the medium- to fine-grained, dark-green coloured, often banded rock consists of amphibole + plagioclase + clinozoisite + titanite ± quartz ± biotite ± garnet ± epidote ± chlorite.

Orthogneiss is present as lenses, often associated with amphibolite. It has the typical appearance of an augen-gneiss with the assemblage quartz + K-feldspar + plagioclase ± biotite ± muscovite ± chlorite.

4.2.3 Geochemistry and Sr-isotopy of marble from the Schenna unit

We investigated three marble samples to compare them with the marbles of the surrounding units and to test if they preserved their original seawater Sr-isotopic ratio. These samples were taken from a white – bright grey marble showing partly distinct layering in the cm-dm range caused by changes in silica content (Fig. 5b). The chemical compositions are given in Appendix Table A1. All three samples yield MgO contents <1 wt%, therefore the rocks are classified as calcareous marbles. Based on the chemical analysis, the white marble sample (S097) is characterised by an assemblage of 99% calcite and about 1% quartz. The trace element results show very different Ba contents, i.e. <10 (HM314), 250 (S143) and 1210 ppm (S097) respectively. This argues for a variable presence of Ba-bearing minerals such as barite and kinoshitalite (Ba-rich mica). The samples show Sr-contents in the range of 178 to 227 ppm. Two of them are characterised by low Rb-contents ≤2 ppm, whereas sample S143 contains 6 ppm Rb. The samples with <2 ppm Rb are suitable for an approximation of the primary Sr-isotopic ratio, while in S143 radiogenic 87Sr from the post-depositional decay of 87Rb will have disturbed the primary values. The measured Sr-isotopic ratios are 0.709167±0.000005 (S097) and 0.712403±0.000061 (HM314).

4.3 Geothermobarometry

Geothermobarometric investigations were performed on garnet-bearing metasediment lithologies from the Schenna and Hirzer unit.

4.3.1 Multi-equilibrium geothermobarometry

For the calculations in the system K_2O-Na_2O-CaO-FeO-MgO-Al_2O_3-SiO_2-H_2O (KNCFMASH) the program THERMOCALC v.3.21 (Holland and Powell, 1998) and the averagePT mode have been used. In the „averagePT" mode, the thermodynamics of an independent set of reactions from an internally-consistent thermodynamic dataset between the end-members of the mineral assemblage (assumed to have been in equilibrium) is combined statistically (by "least squares") to give a P-T result. The phase components used for the calculations in sample 97c were: pyrope (py), grossular (gr), almandine (alm), phlogopite (phl), annite (ann), eastonite (east), anorthite (an), albite (ab), muscovite (mu), paragonite (pa), celadonite (cel) and quartz (q). This leads to the calculation of the four linearly independent H_2O-absent equilibria:

(1) 3 eastonite + 6 quartz = pyrope + phlogopite + 2 muscovite
(2) phlogopite + eastonite + 6 quartz = pyrope + 2 celadonite
(3) pyrope + grossular + muscovite = phlogopite + 3 anorthite
(4) pyrope + annite = almandine + phlogopite

The calculations for two datasets of sample 97c from the Schenna unit yield P-T conditions of 0.59 ± 0.14 GPa and 630 ± 100°C and 0.58 ± 0.14 GPa and 603 ± 99°C. Adding sillimanite to the calculations yields the following independent set of reactions:

(5) grossular + quartz + 2 sillimanite = 3 anorthite
(6) 3 eastonite + 6 quartz = pyrope + phlogopite + 2 muscovite
(7) 7 phlogopite + 12 sillimanite = 5 pyrope + 3 eastonite + 4 muscovite
(8) pyrope + annite = almandine + phlogopite

The resulting calculations for two datasets of sample 97c yield similar P-T conditions of 0.54 ± 0.14 GPa and 596 ± 99°C and 0.52 ± 0.14 GPa and 568 ± 96°C.

In samples MM2b and MM16 representing kyanite-bearing paragneisses from the Hirzer unit the following linearly independent H_2O-absent equilibria were calculated:

(9) 3 eastonite + 6 quartz = pyrope + phlogopite + 2 muscovite
(10) grossular + 2 kyanite + quartz = 3 anorthite
(11) pyrope + 3 eastonite + 4 quartz = 3 phlogopite + 4 kyanite
(12) annite + 3 anorthite = grossular + almandine + muscovite

Sample	Lithology	Tectonic unit	Rb [ppm]	Sr [ppm]	87Rb/86Sr	87Sr/86Sr	± 2σ	Age ± 2σ [Ma]
MM12 (WR)	paragneiss	Schenna	114.8	76.11	4.3795	0.737005	0.000008	**213.6 ± 2.1**
MM12 (Bt)			498.7	6.098	250.53	1.30538	0.000092	
MM11 (WR)	paragneiss	Schenna	83.94	125.3	1.9417	0.722267	0.000004	**162.4 ± 1.6**
MM11 (Bt)			482.5	7.66	189.19	1.094515	0.000035	
MM10b (WR)	paragneiss	Hirzer (Masul shear zone)	93.61	266.6	1.0171	0.718634	0.000004	**139.9 ± 1.6**
MM10b (Bt)			441.1	3.996	354.88	1.841164	0.000029	
WBS38 (WR)	paragneiss	Hirzer	132.2	96.52	3.9746	0.732335	0.000004	**223.0 ± 2.2**
WBS38 (Bt)			328	4.653	217.45	1.380832	0.000043	
MM02 (WR)	paragneiss	Hirzer	204.2	180.6	3.2758	0.717424	0.000003	**269.7 ± 2.7**
MM02 (Bt)			367	4.974	232.1	1.595472	0.000006	
MM07 (WR)	orthogneiss	St. Leonhard	131.8	251.5	1.5178	0.719356	0.000003	**345.7 ± 3.4**
MM07 (Bt)			205.6	2.902	227.65	1.832105	0.000006	

Table 1: Results of the Rb/Sr whole rock (WR) and biotite (Bt) analyses as well as calculated age assuming an error of 1% on the $^{87}Rb/^{86}Sr$ ratio. The samples are ordered from South to North (Fig. 1) which corresponds to a bottom to top order in the nappe stack.

The resulting P-T conditions for three datasets of sample MM2b are 0.39 ± 0.11 GPa and 510 ± 72°C, 0.50 ± 0.15 GPa and 528 ± 92°C and 0.55 ± 0.14 GPa and 577 ± 86°C. Those of sample MM16 are 0.52 ± 0.12 GPa and 535 ± 75°C.

4.3.2 Calcite-dolomite geothermometry

For calcite-dolomite geothermometry the calibration of Anovitz and Essene (1987) was used for samples from the Schenna unit. The BSE image of the selected crystals is shown in Figure 9, the analytical data are presented in Appendix Table A4 and the calculations in Appendix Table A5. Two samples (S097, WBS29) yield temperatures below 335°C, namely 300-335°C (sample SO97) and 130-275°C (WBS29). Sample WBS36 experienced temperatures in the range of 390-425°C. Two clusters of temperatures were obtained from sample WBS35: Mg-rich calcite cores yield temperatures of 525-585°C and Mg-poor rims yield 300-430°C.

4.4 Rb/Sr biotite ages

Results of isotopic measurements on whole rock powders and biotite separates are given in Table 1; the plots of the age regression lines are provided in the Appendix Figure A1. In Figure 10 the new Rb/Sr biotite data are reported in map view together with the literature data from biotite and white mica. Two samples from the Schenna unit (MM11 and MM12) were investigated. Sample MM11, a mylonitic paragneiss collected from the structural uppermost part at the margin towards the Masul shear zone yield an age of 162 ± 1.6 Ma. From the central part of the unit, away from prominent ductile shear zones, an age of 214 ± 2.1 Ma was determined for paragneiss sample MM12. Unfortunately, in the vicinity of the marble layer, biotite is strongly chloritised, thus no suitable samples for Rb/Sr dating were obtained. Three new Rb/Sr biotite ages were obtained from the Hirzer unit. Sample MM02 was collected close to the northern (upper) limit of the unit and yields an age of 270 ± 2.7 Ma. The second sample (WBS38) from the central part yields a somewhat younger age of 223 ± 2.2 Ma. For sample MM10, coming from the Masul shear zone in the southernmost corner of the Hirzer unit, an age of 139.9 ± 1.4 Ma was calculated. An age of 346 ± 3.4 Ma has been determined for paragneiss of sample MM07 from the southernmost corner of the St. Leonhard unit, adjacent to the Fartleis fault. The biotite from this sample was slightly altered. This is also indicated by the lowest Rb-content. Therefore, the age must be treated with some caution.

5. Discussion

The first part of this chapter deals with aspects on the lithologies of the Schenna and Hirzer units. After that, topics concerning the whole MMNS and the relation of the MMNS to other parts of the Austroalpine unit are discussed.

5.1 The Schenna unit

5.1.1 The spatial extent of the Schenna unit

On the map sheet CARG 13-Meran/Merano (AA.VV., 2010) the Schenna unit and Masul shear zone are cut off by the MMF on the eastern border of the map sheet, between the locality Muls in Sarntal (Mules in Sarentino) and the summit Grubenkopf (Monte delle Fosse). However,

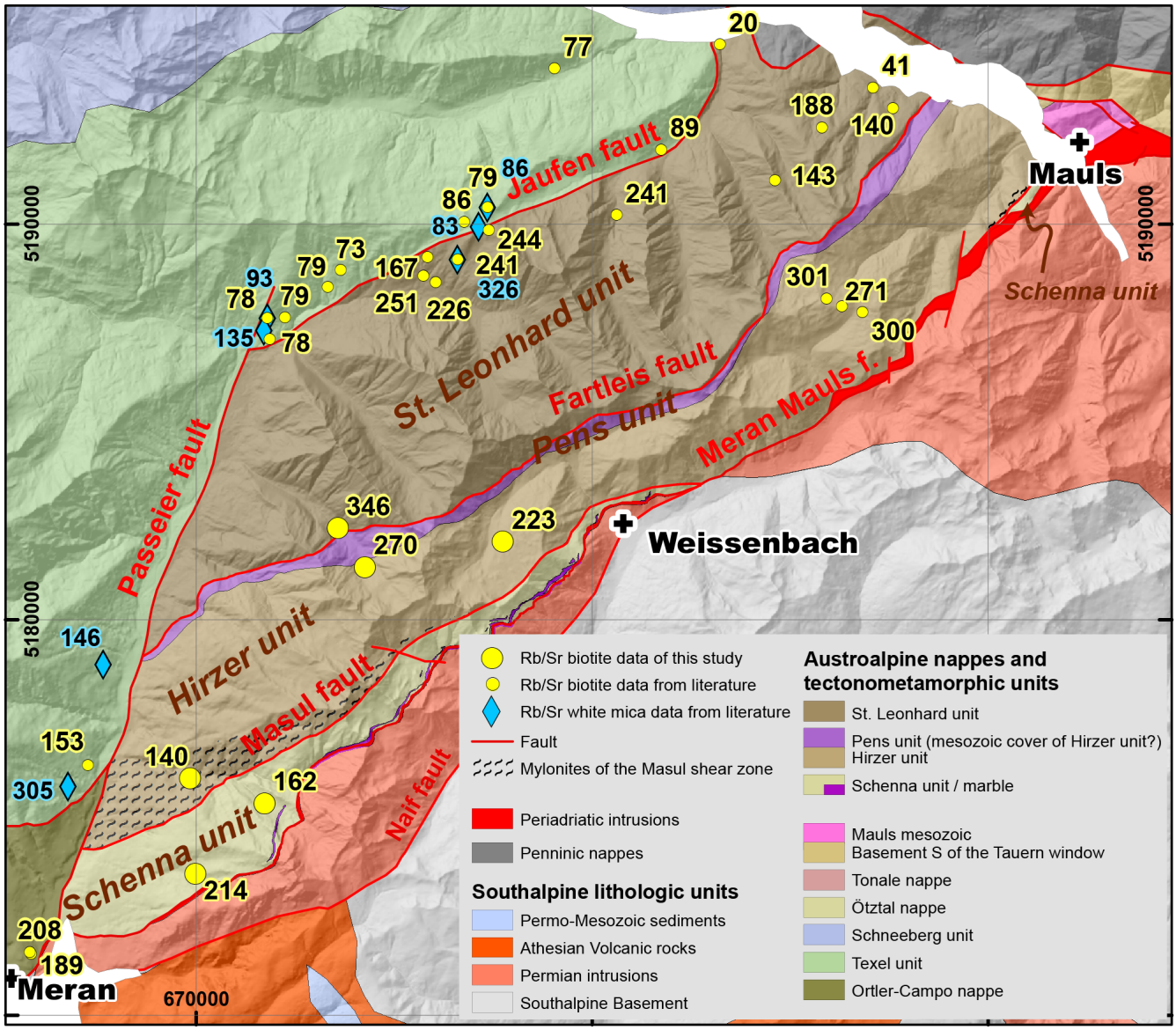

Figure 10: Compilation of Rb/Sr bt data from this study and from the literature. Ages are given in Ma.

detailed mapping in the frame of the present study shows that the marble belt can be traced further NE-wards to the village Weissenbach (Rio Bianco) (Fig. 2). Sillimanite-bearing paragneiss (Fig. 11a) and a pegmatitic dike (Fig. 11b), the most characteristic lithologies of the Schenna unit, were even found east of the Pens (Pennes) pass near Mauls (Fig. 2). At the top, this slice is delimitated and overlain by fine-grained, quartz-rich mylonites representing the Masul shear zone (Fig. 11c). The occurrence of the Schenna unit as two triangle-shaped slices NE and SW of the Pens pass is the result of intersection between the Masul shear zone, the MMF and the topography. At the Pens pass, the Schenna unit is hidden in the subsurface and the overlying Hirzer unit crops out in direct contact with the Southalpine unit (Fig. 12).

5.1.2 The marble horizon

Apart from the Mesozoic carbonates present in the Pens unit the mylonitic marble layer along the southeastern border of the Schenna unit is the only occurrence of carbonate rocks within the MMNS. Its occurrence close to and parallel to the MMF is truly remarkable. Main questions concerning the marble layer are its stratigraphic age and its tectonic position. From a tectonic point of view there are three possibilities:

1. The marble layer could represent an integral part of the Schenna unit and therefore a pre-Variscan sediment with an amphibolite-facies Variscan and/or Permian imprint and an Eoalpine overprint.
2. It might also represent Mesozoic sediments highly deformed and partly infolded along the MMF. In this case, they should record only a weak metamorphic

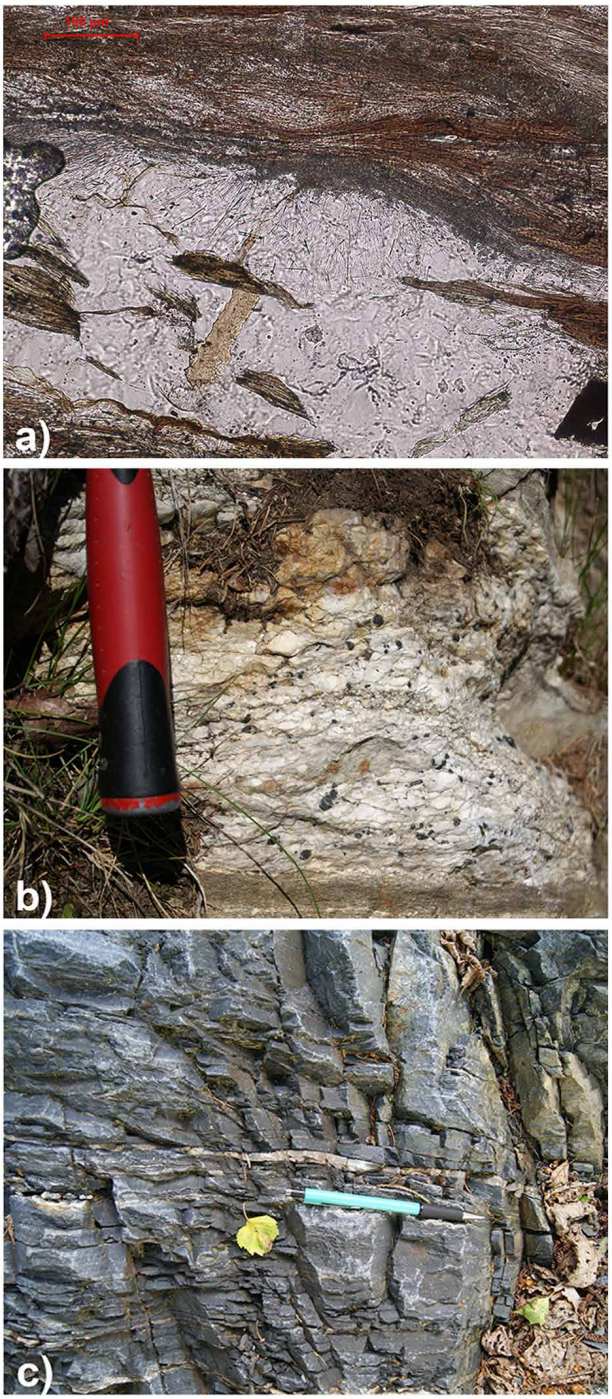

Figure 11: (a) sample A95; thin section of paragneiss with sillimanite growing statically on biotite as fibrolite; (b) close up of a pegmatite occurring on outcrop A94; (c) fine grained mylonite on outcrop A93. For coordinates see table in Appendix Table A2

overprint. If they represent the Mesozoic cover of the Schenna unit, the latter would be in a tectonically inverted position today.

3. Furthermore, the marble layer could represent a tectonic slice of a marble-bearing unit from the surrounding, e.g. the Schneeberg unit or Laas unit (Pomella et al., 2016).

Detailed mapping (Fig. 8) showed that a very vague correlation between the three investigated sections can be made but no overall clearly discernible stratigraphic succession can be identified. However, even if it is intensely deformed, it is unlikely that the repetition of the calcite marble, dolomite marble and quartzite layers is only due to internal slicing and folding. At least partly it seems to be a primary sedimentary feature.

The marble within the Schenna unit shows evidence for a polymetamorphic overprint since geothermometric calculations using Mg-rich calcite cores showed high temperatures of 525-585°C and the Mg-poor rims yielded 300-430°C. The calcite-dolomite results of the rims fit approximately the temperatures reached during Eoalpine metamorphism that have to be in the range of the closure temperature of the Rb/Sr system in biotite, which is about 300±50°C (Satir, 1975; Del Moro et al., 1982; Thöni, 1983; Spiess, 1995). The higher temperatures from the cores are the result of a pre-Alpine (Permian or Variscan) event. Since the zoning of calcite can be interpreted as result of two metamorphic events, it excludes the interpretation of the marble horizon as a monometamorphic Mesozoic cover unit that experienced only a single, Eoalpine metamorphic overprint.

The determined $^{87}Sr/^{86}Sr$ isotopic ratios (0.709167±0.000005 and 0.712403±0.000061) are strongly different and do not correlate to the oceanic sea water curve (McArthur et al., 2001) for Phanerozoic time, except for the lower value, which fits to the time interval of 495-500 Ma (late Cambrian). However, such a deposition age can be ruled out, due to regional considerations. Therefore, an alteration of the $^{87}Sr/^{86}Sr$ isotopic ratios by radiogenic ^{87}Sr from the surrounding metapelitic country rocks is most likely. According to Pomella (2010) the $\delta^{18}O$ and $\delta^{13}C$ values of the marble layer indicate a complete recrystallisation during mylonitisation and the occurrence of uncommon assemblages with Ba-enriched minerals (Degenfelder et al., 2016) argues for metasomatic rejuvenations.

Due to the structural and metasomatic overprint it is not possible to compare the marble to those of the surrounding units (e.g. Laas marble and Töll marble from near to Meran of the Campo nappe and marble from the Schneeberg unit) with respect to the primary signatures (Puhr et al., 2009). As the investigated marble is characterised by a polyphase metamorphic history, it differs from those of the Schneeberg unit, since the latter experienced only a single amphibolite-facies Eoalpine metamorphic imprint (Konzett and Hoinkes, 1996).

Concluding, based on the available data it is most likely that the marble layer discussed in here is of pre-Mesozoic age and represents an integral part of the Schenna unit.

5.1.3 The pre-Alpine metamorphic evolution of the Schenna unit

According to thermochronological data from the literature and the new data reported in here (see

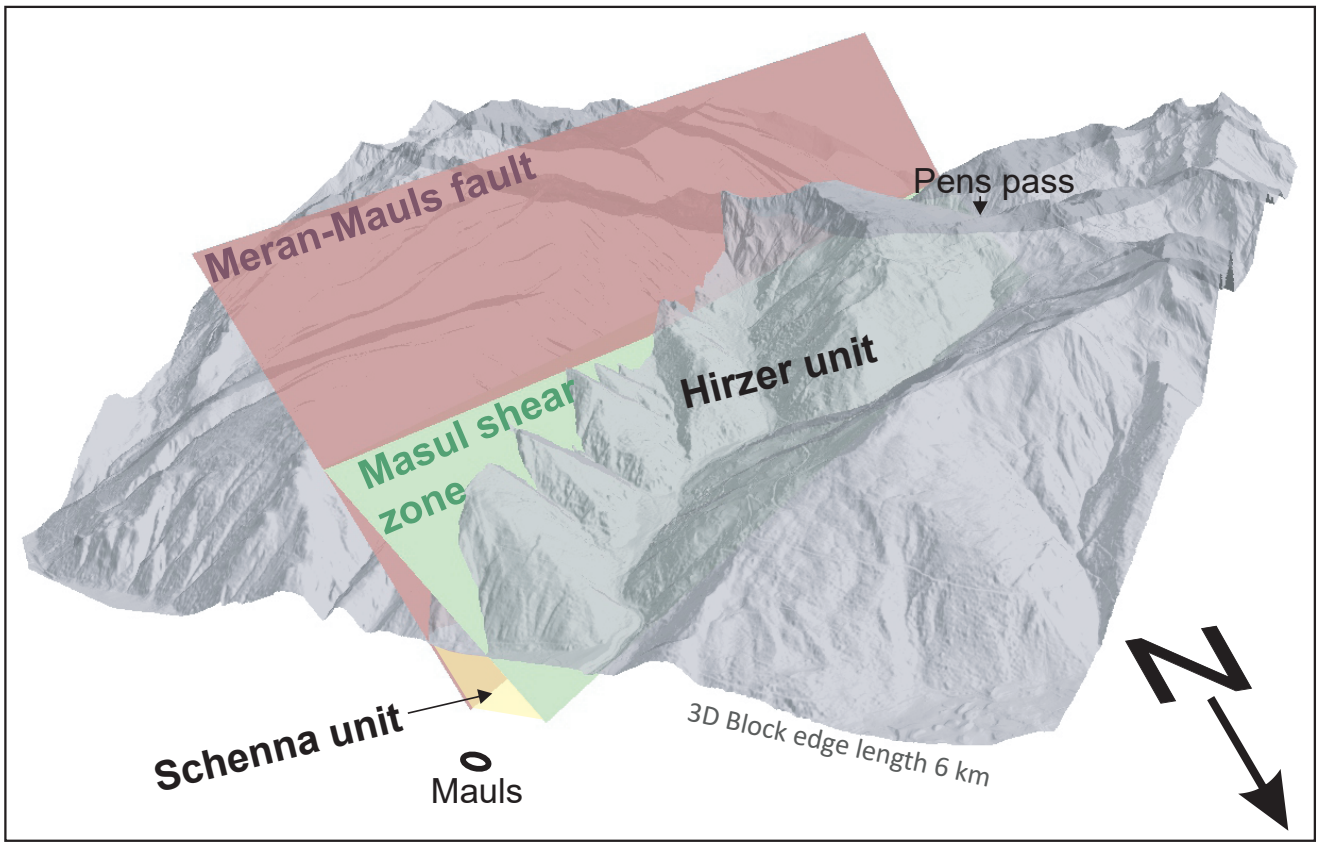

Figure 12: The figure shows the intersection of the simplified Masul shear zone and Meran-Mauls fault planes, enclosing the Schenna unit, with the topography in the Pens pass area.

below) the Eoalpine metamorphic conditions in the Schenna unit reached lowermost greenschist-facies only. Consequently, the observed upper greenschist- to amphibolite-facies mineral assemblages formed prior to the Eoalpine event. For the Schenna unit Bargossi et al. (2010) identified a two-stage pre-Alpine metamorphic evolution: first, an amphibolite-facies assemblage developed in the stability field of garnet, followed by static growth of sillimanite. However, there are three possibilities for the timing of these stages: they might have formed during a single clockwise P-T-t path during the (1) Variscan or alternatively the (2) Permian HT/LP event, or (3) they formed by a polyphase evolution with an earlier Variscan assemblage overprinted during the Permian HT/LP event. From individual Austroalpine units all three possibilities are documented (e.g. Tropper and Recheis, 2003; Schuster et al., 2004; Thöni and Miller, 2009). Due to the lack of geochronological data neither the timing of garnet growth nor the formation of the sillimanite bearing assemblage of the Schenna unit is known until now. However, the association of sillimanite bearing paragneiss with Permian pegmatite dikes in addition to Permian and Triassic cooling ages (see below) are typical features of Austroalpine units with a proven Permian overprint (Schuster et al., 2001). According to Schuster and Stüwe (2008), the area from which the rock units under discussion were formed, was affected by lithospheric extension during Permo-Triassic times, thus leading to widespread magmatism and HT/LP metamorphism. Metamorphism was characterised by a high geothermal gradient of more than 40°C/km, thus reaching amphibolite- to granulite-facies conditions. Peak metamorphism was reached at about 270 Ma and subsequently the rocks were not exhumed but cooled down until approximately 190 Ma, when the steady state geotherm was reached again.

The pegmatite dikes in the Schenna unit are hitherto still not dated. However, as all pegmatite fields in adjacent Austroalpine units show consistent ages of 250-285 Ma a Permian age is strongly indicated (e.g. Bockemühl, 1988; Schuster et al., 2001; Mair and Schuster, 2003; Sölva et al., 2003; Knoll et al., 2018). The P-T conditions determined for the sillimanite bearing assemblage in the Schenna unit are 0.52-0.59 GPa and 570-630°C. They agree well with the data of the Permian event in the Alps as summarized in Kunz et al. (2018). Also the Rb/Sr biotite ages do not contradict a Permian metamorphic imprint in the Schenna unit.

5.2 Thermochronological evolution of the MMNS

In the following section the new Rb/Sr biotite ages are discussed in conjunction with existing literature data (Fig. 10). These ages are interpreted as cooling ages with an assumed blocking temperature of 300±50 °C (Jäger

and Niggli, 1967; Thöni, 1996) but also being aware of problems associated with the concept of a strictly defined blocking temperature (e.g. Del Moro et al., 1982). The age measured on a paragneiss characterised by a Permian sillimanite-bearing mineral assemblage, representative for the central part of the **Schenna unit** sufficiently away from prominent ductile shear zones yielded 214 Ma (sample MM12). This Late Triassic age is interpreted as a result of slow cooling after the Permian event, similarly as observed in other Austroalpine units (Schuster et al., 2001; Schuster et al., 2015). A younger age of 162 Ma (sample MM11) was obtained from a mylonitic paragneiss from the margin of the Masul shear zone. The latter age most likely reflects partial resetting of the Rb/Sr system in biotite during mylonitic deformation. From the northeastern part of the **Hirzer unit** along the Pens pass road Del Moro et al. (1982) published two Rb/Sr biotite ages of 300 and 301 Ma and an additional age was published by Thöni (1981) which is 271 Ma. The new Rb/Sr biotite ages from this study were measured on samples further to the southwest, where no age data were available until now. The obtained Permian age of 270 Ma (sample MM02) comes from the northern (upper) part of the unit, whereas a second age from the central part yields a Late Triassic age of 223 Ma (sample WBS38). In general, these data indicate an age rejuveination trend towards the southeast. The ages of ca. 300 Ma represent cooling ages after the Variscan metamorphic peak, whereas the younger age might reflect slow cooling of the unit after the Permian LP/HT event or a partial rejuvenation during the Eoalpine event. Following Pomella et al. (2012) who interpreted the Permotriassic sedimentary succession of the Pens unit as a (para)autochthonous Mesozoic cover of the Hirzer unit, a Permian imprint of more than 350 °C directly below the base of the sedimentary succession is unlikely and therefore we tend to prefer the interpretation as a partial rejuvenation during the Eoalpine event. Sample MM10 was collected from the southernmost corner of the Hirzer unit, within the **Masul shear zone**. Bistacchi et al. (2008) described km-thick ultramylonites showing greenschist-facies conditions which postdate the Variscan metamorphic overprint. The earliest Cretaceous age of about 140 Ma thus might reflect mylonitization along the Masul shear zone, however, further investigations are necessary to support this possible interpretation. The oldest age of 346 Ma (sample MM07) comes from the southernmost corner of the **St. Leonhard unit**, adjacent to the Fartleis fault. The biotite from this sample also was altered, therefore the result must be treated with some caution. However, the Variscan age indicates that this part of the basement did not experience temperatures above 350 °C after the Variscan amphibolite-facies metamorphic overprint. Also shearing along the nearby Fartleis fault did not provide thermal conditions high enough to reset the Rb/Sr system of biotite in this sample. Along the Jaufen fault, six Rb/Sr biotite ages were published from the St. Leonhard unit (Del Moro et al., 1982; Spiess, 1995). With one exception (167 Ma) these data plot between 226-251 Ma. The north-eastern part of the St. Leonhard unit, close to the Jaufen fault (e.g. Viola et al., 2001; Luth and Willingshofer, 2008; Pomella et al., 2012; Luth et al., 2013; Pomella et al., 2016), is characterised by even younger Rb/Sr biotite ages ranging between 190 and 140 Ma. To the north of the fault the Texel unit yields exclusively Late Cretaceous (73-90 Ma) cooling ages postdating the Eoalpine metamorphic peak (Del Moro et al., 1982; Spiess, 1995). As there are no other indications for a Permian overprint within the St. Leonhard unit, we follow the interpretation by Spiess (1995) who explained the scattering Rb/Sr biotite ages caused by an Eoalpine thermal overprint reaching lowermost greenschist-facies conditions. Close to the north-eastern boundary of the St. Leonhard unit, very young ages of 20 Ma (Spiess, 1995) and 41 Ma (Del Moro et al., 1982) were reported, indicating at least partial resetting during a Neoalpine overprint. This reset is thought to be due to the temperature anomaly caused by the rising Penninic and Subpenninic units within the Tauern Window and/or due to tilting of the St. Leonhard unit, exposing deeper structural levels in the NE (Pomella et al., 2012; Bertrand et al., 2017; Klotz et al., 2019).

5.3 Formation of the Meran-Mauls nappe stack

There is no doubt that the individual nappes of the MMNS were arranged in their present configuration during post-Permian tectonic movements, because Permo-Triassic sediments occur along the Fartleis fault and the Permian amphibolite-facies metamorphic imprint of the Schenna unit is cut off along the Masul shear zone. However, the age and kinematics of the two major internal structures are still unclear. With respect to the kinematics it is important to note, that the recent dip of these structures towards northwest is most probably a late feature related to deformation associated with the indentation of the Southalpine unit. As the degree of rotation during this process is still unknown, any attribution of these structures to a thrust or normal fault remains problematic.

According to Bistacchi et al. (2008), the Masul shear zone might be the result of strain partitioning along the hanging wall of the Meran-Mauls fault during exhumation of the Austroalpine units in front of the edge of the Dolomites indenter, with the rigid mass of the Permian intrusion directly at the contact (see Fig. 1). Based on literature the indentation started at about 23 Ma (Scharf et al., 2013), or at least later than approximately 28 Ma (Pomella et al., 2011; Pomella et al., 2012; Schneider et al., 2015). This would imply an Oligocene-Miocene age of shearing under (upper) greenschist-facies conditions at the Masul shear zone and a contemporaneous activity together with the MMF. However, two arguments argue against this interpretation. Firstly, the two clusters of mylonitic lineation of the Masul shear zone exhibit a clear spatial pattern, whereby the shallow NE dipping strike slip lineation is restricted to outcrops close to the intersection with the MMF. This shallowly NE dipping strike slip lineation is similar to that of the dextral

strike slip phase along the MMF, which predates the indentation (Pomella et al., 2011). However, it cannot be excluded that it is in fact not the original lineation of the Masul shear zone mylonite, but the result of a later local overprint. This interpretation would imply that the Masul shear zone is older than the dextral strike slip phase along the MMF. Secondly, mylonites of the Masul shear zone formed at (upper) greenschist-facies conditions (Bistacchi et al., 2008). At these conditions, a total reset of the Rb/Sr isotopic system in biotite to Oligocene-Miocene age values would be expected, but the measured age is earliest Cretaceous (ca. 140 ± 1.6 Ma, sample MM10). Assuming this age is meaningful it is difficult to correlate it with Eoalpine thrusting, because no nappe stacking is known at that time from the Austroalpine unit (e.g. Pomella et al., 2016). It might therefore be correlated with latest Jurassic/earliest Cretaceous strike slip faulting as is indicated by the Austroalpine units further to the east (e.g. Schuster et al., 2015). Often these faults have been tilted and reactivated as reverse faults during Eoalpine and/or Neoalpine deformation. However, further investigations are necessary to clarify these questions.

Along the second important fault within the MMNS, the Fartleis fault, the crystalline basement of the St. Leonhard unit overlays the basement rocks and Permotriassic sediments of the Pens unit. The entire Pens unit is deformed and boudinaged and Bargossi et al. (2010) described it therefore as a NW dipping, transpressive shear zone. Brittle deformation is intense, especially along the upper boundary of the unit. The Permotriassic sediments are internally folded, boudinaged and stacked. The distribution of the stretching lineation (Fig. 2) shows a girdle distribution and in the field it was not possible to define a temporal relationship between different orientations of lineation. Therefore, it is still unresolved if the variation is due to multiple deformation phases in different stress fields or if the girdle distribution is an effect of the intense boudinage and brittle overprint of the shear zone. There is also no detailed information about the timing of deformation. As both, the Pens unit and the Fartleis fault are cut off by the Miocene Passeier- (Müller et al., 2001; Pleuger et al., 2012) and Sprechtenstein-Mauls faults (Bistacchi et al., 2010; Schiavo et al., 2015) they both may have been active during the Eoalpine event in the Cretaceous and/or in Oligocene time. Figure 13 shows a simplified NW-SE oriented cross section based on the model presented by Pomella et al. (2016) and is intended to illustrate our interpretation of the position of the MMNS within the Austroalpine nappe stack.

5.4 Correlation of the MMNS with other elements of the Austroalpine unit

As the MMNS is bounded by Oligocene-Miocene faults, its former spatial relation to other elements of the Austroalpine unit is of interest and discussed in this chapter. Two aspects are important for possible correlations: firstly, lithostratigraphic aspects, including the lithological content, stratigraphic age and petrological characteristics, which are the result of the metamorphic history of the rock units, and secondly tectonic aspects like the structural position within the nappe stack and the timing of emplacement along certain structural elements. With respect to lithostratigraphy the Hirzer and St. Leonhard units are dominated by paragneiss with orthogneiss intercalations, which experienced a dominating Variscan and a weak Eoalpine overprint. Comparable complexes are present in parts of the Ortler-Campo nappe and the Tonale nappe (e.g. Avanzini et al., 2007; Martin et al., 2009a), in the western part of the Ötztal nappe (e.g. Tropper and Hoinkes, 1996), south of the Tauern window in the Antholz/Anterselva unit (Cesare et al., 2021) as well as in the southern Defereggen Alps (e.g. Borsi et al., 1978; Heinisch and Schmidt, 1984; Schulz et al., 2008), and in the Drau Range (e.g. Heinisch et al., 1983). However, as the lithologies and assemblages are very common and as there are no data on the detrital zircon spectra of the paragneiss and no detailed geochemical and age information on the orthogneiss intercalations, specific correlations are not possible at the moment. In contrast, the Schenna unit shows more pronounced lithological characteristics: a) it is composed of sillimanite-bearing paragneiss, marble and most probably Permian pegmatite dikes; b) it seems to be affected pervasively by the Variscan amphibolite-facies event, a Permian HT/LP event and a lowermost greenschist-facies Eoalpine metamorphic overprint.

Nearby Complexes with characteristics similar to the Schenna unit are (Fig. 1):

1) the Tonale unit within the Tonale nappe
2) the Laas (Lasa) unit within the Ortler-Campo nappe
3) the Matsch (Mazia) unit
4) the Strieden Complex Kreuzeck Mountains (Schuster et al., 2001) and equivalents of the Rappold Complex (Petzeck-Rotenkogel Complex) in the Deferegger Alps (e.g. Stöckhert, 1984, 1985; Schulz et al., 2008),

Taking into account also the tectonic aspects, a more precise correlation is possible. Within the southern part of the Austroalpine unit Hoinkes et al. (1999) introduced the so called "Southern border of Alpine Metamorphism" (SAM). Units to the north of the SAM are affected be an intense (amphibolite- to eclogite-facies) Eoalpine metamorphic imprint, whereas to the south only a weak (lower greenschist-facies) Eoalpine overprint can be detected. In Schmid et al. (2004) these Eoalpine weakly metamorphosed units to the south of the SAM are summarised in the Drauzug-Gurktal nappe system and the MMNS represents a part of it. From a tectonic point of view, only units within the Drauzug-Gurktal nappe system can be laterally correlated with the MMNS.

At 1) To the Southwest of the MMNS, the Tonale nappe in the hanging wall of the Pejo fault is subdivided into a) the Tonale unit, forming the external part of a wide synform with the b) Ulten unit in its core (Andreatta, 1948; Godard et al., 1996; Viola et al., 2003; Avanzini et

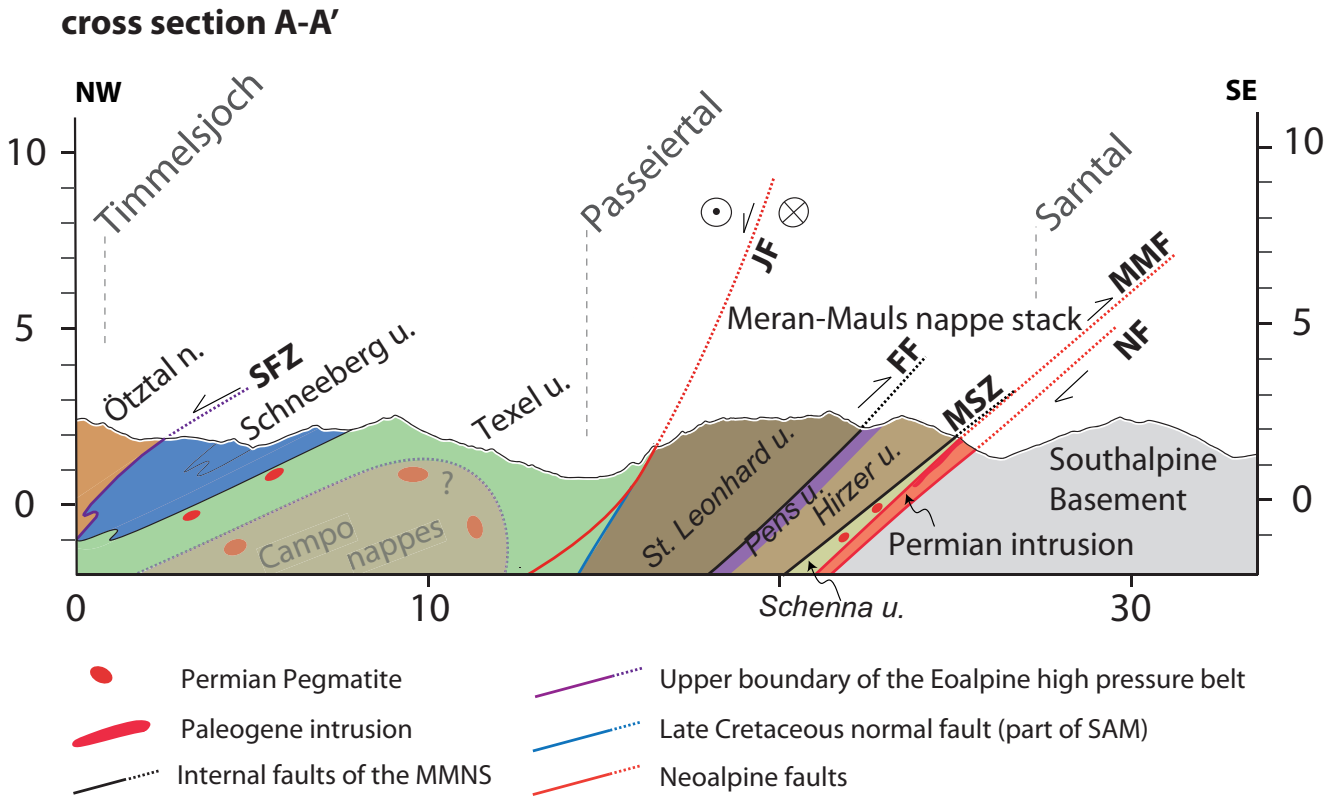

Figure 13: Modified excerpt of Figure 3 in Pomella et al. (2016). The position of the cross section is given in Figure 2. For a detailed evolution model in a wider geodynamic context see Figure 2 in Pomella et al. (2016). SFZ: Schneeberg fault zone, JF: Jaufen fault, FF: Fartleis fault, MSZ: Masul shear zone, MMF: Meran Mauls fault, NF: Naif fault

al., 2007; Martin et al., 2009b). The Tonale unit shares the main lithological characteristics with the Schenna unit, whereas the lithologic content of the Ulten unit (Godard et al., 1996) is fundamentally different compared all subunits of the MMNS.

At 2) The Laas unit is similar to the Schenna unit from a lithological point of view with its occurrence of Permian pegmatite, amphibolite and the famous Laas marble. According to Mair et al. (2007) the Laas unit forms the lowermost unit of the Ortler-Campo nappe, which is attributed to the Silvretta-Seckau nappe system by Schmid et al. (2004). To the north, towards the Ötztal nappe, it is bordered by the Schlinig fault and Vinschgau shear zone and to the south by the Laas fault. It experienced upper greenschist-facies Eoalpine metamorphism and based on geochemical and isotope studies, the massive marble intercalations are most probably the continuation of Austroalpine units to the north of the SAM (Puhr et al., 2009; Unterwurzacher, 2009). Nevertheless, the tectonic attribution of the Laas unit to the Silvretta-Seckau nappe system excludes a lateral correlation with the Schenna unit (Drauzug-Gurktal nappe system).

At 3) North of the Vinschgau valley, the Matsch unit (e.g. Hammer, 1912; Potro, 1982; Schuster et al., 2001; Habler et al., 2009) shares many lithological characteristics with the Schenna unit: the dominant lithologies are micaschist and paragneiss often containing sillimanite and/or garnet. The occurrence of pegmatite is common, amphibolite, orthogneiss and marble occur in lenses. Habler et al. (2009) report an early Permian age (280-263 Ma; Sm-Nd on garnet) for the pegmatite. The Matsch unit forms a nappe on top of the southwestern Ötztal nappe and these nappes are separated by a ductile shear zone and together form a wide synform folded along an approximately W-E oriented fold axis (explanatory notes CARG Map sheet 012 Schlanders/Silandro; in prep.). Only the Matsch unit experienced Permian metamorphism but both units experienced an Eoalpine metamorphic overprint under greenschist-facies conditions with a well-constrained P-T gradient to higher metamorphic conditions towards the east (Schuster et al., 2001; Habler et al., 2009; Bernabè et al., 2017). In the classification scheme of Schmid et al. (2004), the Matsch unit is part of the Ötztal-Bundschuh nappe system. However, this classification is problematic, because all other elements of this nappe system are characterised by a Permomesozoic cover, indicating a position in the uppermost part of the crust during the Permian thermal event, whereas the occurrence of Permian pegmatite indicates a deep crustal position for the Matsch unit at that time, comparable to the Schenna unit. Therefore, also an attribution of the Matsch unit to the Drauzug-Gurktal nappe system must be taken into account. Precise timing of nappe stacking would certainly help to

assign the position and tectonic affiliation of the Matsch unit in the nappe scheme of Schmid et al. (2004), but until now no data are available.

At 4) To the east, the Drauzug-Gurktal nappe system is composed of several nappes and slices (e.g. Schulz et al., 2008; Schuster et al., 2015). In general, they represent a section through the Permomesozoic crust, which is tilted and folded by E-W oriented axes during the Cretaceous (Schuster et al., 2001). At the base of the nappe stack, units affected by the Permian HT/LP event are present; the Strieden Complex in the Kreuzeck Mountains and the eastern part of the Deferegger Alps (Michelbach valley) show a very similar lithological composition and metamorphic evolution as the Schenna unit, whereas the Jenig Complex in the Gailtal Alps is characterised by the Permian HT/LP overprint only. Structurally above, different Variscan metamorphic units with Ordovician orthogneiss bodies occur, partly with a Permomesozoic cover. In some places these units are separated or cut by several hundred meters wide, steeply inclined shear zones, which might have formed during latest Jurassic-earliest Cretaceous strike-slip tectonics (Schuster et al., 2015; Griesmeier et al., 2019). These faults can be compared to the Masul shear zone based on their estimated age and tectonic position, but until now no clear evidence for an important strike slip deformation along the Masul shear zone could be found in the field.

6. Conclusions

According to the data presented above the following conclusions concerning the tectonostratigraphy of the MMNS can be drawn:

- The MMNS consists of three nappes separated by the Masul shear zone and Fartleis fault. The whole nappe stack experienced only a weak, lower greenschist-facies Eoalpine (Cretaceous) metamorphic overprint. This is indicated by partly resetting of the Rb/Sr system in biotite and calcite-dolomite geothermometry.
- The lowermost nappe is formed by the Schenna unit, characterised by sillimanite-bearing paragneiss, partly kinoshitalite-bearing calcite and dolomite marble and most probably Permian pegmatite dikes. It is characterized by an amphibolite-facies Permian metamorphic overprint. Permian P-T conditions of the Schenna unit are 0.52-0.59 GPa and 570-630°C.
- The Schenna unit can be traced from Meran until Mauls with a small gap in the area of the Pens pass (Penser Joch) due to the intersection of the bounding faults with the topography.
- For the marble layer near the base of the Schenna unit, a pre-Mesozoic age is indicated through a polymetamorphic history. Calcite-dolomite geothermometry yielded temperatures of 500-600°C (upper greenschist-facies to amphibolite-facies) during a pre-Eoalpine metamorphic event, whereas for the rims temperatures of 300-430°C (lower greenschist-facies) were determined, indicating the later Eoalpine metamorphic overprint.
- Above the Schenna unit, a nappe composed of the Hirzer unit and the overlying Pens unit, including remnants of a Permotriassic cover sequence is present. Biotite Rb-Sr ages of the basement rocks (paragneiss and orthogneiss) as well as geothermobarometry are indicative of a pervasive Variscan amphibolite-facies metamorphic overprint.
- The broad Masul shear zone mainly consists of mylonized paragneiss of the Hirzer unit overprinted under greenschist-facies conditions. Rb/Sr biotite ages from the mylonites yield 140 ± 2 Ma and therefore the possibility arises that it is related to latest Jurassic - earliest Cretaceous strike slip tectonics.
- Laterally the MMNS and can be correlated with other composite elements of the Drauzug-Gurktal nappe system south of the SAM. The special lithological composition and polymetamorphic evolution of the Schenna unit corresponds either to that of the Tonale unit in the southwest or the Strieden-Complex in the east. The Matsch unit in the west is lithologically and from a metamorphic point of view also very similar, but for this unit the position within the overall Austroalpine nappe scheme is still unclear.

Acknowledgments

This study was funded by the University of Innsbruck, Aktion D. Swarovski KG. We acknowledge Stanislaw Grabala (Geological Survey of Austria) for help with the biotite separation and Monika Horschinegg (University of Vienna) for her help in measuring the Rb and Sr-isotopic ratios. We thank editor Kurt Stüwe for his efforts and the journal reviewers, Georg Hoinkes, Matteo Massironi and Richard Spiess for their constructive comments.

References

AA.VV., 2010. Carta Geologica d'Italia alla scala 1:50.000, Foglio 013 Merano. Servizio Geologico d'Italia - ISPRA. SystemCart, Roma. https://www.isprambiente.gov.it/Media/ carg/13_MERANO/Foglio.html

AA.VV., online first. Carta Geologica d'Italia alla scala 1:50.000, Foglio 009 Anterselva. Servizio Geologico d'Italia - ISPRA. https://www.isprambiente.gov.it/Media/carg/9_ANTERSELVA/Foglio.html

Andreatta, C., 1948. La "Linea di Pejo" nel massiccio dell'Ortles e le sue miloniti. Acta geologica alpina 1, 1-63.

Anovitz, L.M., Essene, E., 1987. Phase equilibria in the system CaCO3-MgCO3-FeCO3. Journal of Petrology 28, 389-415.

Avanzini, M., Bargossi, G.M., Borsato, A., Castiglioni, G.B., Cucato, M., Morelli, C., Prosser, G., Sapelza, A., 2007. Note illustrative della Carta Geologica d'Italia - Appiano foglio 026 SystemCard, Roma.

Baggio, P., Friz, C., Gatto, G.O., Gatto, P., Gregnanin, A., Justin-Visentin, E., Lorenzoni, S., Mezzacasa, G., Morgante, S., Omenetto, E.M., Sassi, F.P., Zanettin-Lorenzoni, E., B., Z., Zulian, T., 1971. Note illustrative della

Carta Geologica D'Italia 1:100.000. Foglio 4 / Merano Nuova Tecnica Grafica, Roma.

Bargossi, G.M., Bove, G., Cucato, M., Gregnanin, A., Morelli, C., Moretti, A., Poli, S., Zanchetta, S., Zanchi, A., Ambrosi, C., Cortini, P., Crottini, A., Macconi, P., Mair, V., Marocchi, M., Montresor, L., Toffolon, G., Tumiati, S., 2010. Erläuterungen zur geologischen Karte von Italien im Maßstab 1:50.000 Blatt 013 Meran, CARG. ISPRA, Istituto Superiore per la Protezione e la Ricerca Ambientale, SystemCart Roma, p. 320.

Baumgarten, B., Folie, K., Stedingk, K., 1998. Auf den Spuren der Knappen. Bergbau und Mineralien in Südtirol. . Tappeiner, Athesia, Bozen.

Bernabè, E., Tropper, P., Fügenschuh, B., Mair, V., Montresor, L., Morelli, C., Moretti, A., Piccin, G., Zanchetta, S., 2017. The polymetamorphic evolution of the Austroalpine basement units (Matsch Nappe, Ötztal Complex) in the Vinschgau/South Tyrol. Mitteilungen der Österreichischen Mineralogischen Gesellschaft 163.

Bertrand, A., Rosenberg, C., Rabaute, A., Herman, F., Fügenschuh, B., 2017. Exhumation mechanisms of the Tauern Window (Eastern Alps) inferred from apatite and zircon fission track thermochronology. Tectonics 36, 207-228.

Bistacchi, A., Massironi, M., Menegon, L., 2010. Three-dimensional characterization of a crustal-scale fault zone: The Pusteria and Sprechenstein fault system (Eastern Alps). Journal of Structural Geology 32, 2022-2041.

Bistacchi, A., Massironi, M., Menegon, L., Zanchetta, S., Zanchi, A., 2008. Late Alpine fault systems in the central-eastern Alps between Merano and Vipiteno: preliminary results. Rendiconti online SGI, 31-36.

Bockemühl, C., 1988. Der Marteller Granit. University of Basel, p. 144.

Borsi, S., Del Moro, A., Sassi, F.P., Zanferrari, A., Zirpoli, G., 1978. New geopetrologic and radiometric data on the Alpine history of the Austridic continental margin south of the Tauern Window (Eastern Alps). Memorie di scienze geologiche 32, 1-19.

Brandner, R., Reiter, F., Töchterle, A., 2008. Überblick zu den Ergebnissen der geologischen Vorerkundung für den Brenner-Basistunnel. Geo.Alp 5, 165-174.

Cesare, B., Cucato, M., Furlanis, S., Keim, L., Mair, V., Mazzoli, C., Meli, S., Morelli, C., Moretti, A., Peruzzo, L., Piccin, G., Sassi, R., Spiess, R., 2021. Note Illustrative della Carta Geologica s'Italia - Anterselva foglio 009. SystemCard, Roma, p 165.

Degenfelder, J., Tropper, P., Costantini, D., Pomella, H., 2016. Mineralogische Untersuchungen der Mischkristallreihe Ba-hältiger Phlogopit - Kinoshitalit in Marmoren aus dem Meran-Mauls Basement. Mitteilungen der Österreichischen Mineralogischen Gesellschaft 162, 47-59.

Del Moro, A., Sassi, F.P., Zirpoli, G., 1982. New radiometric data on the alpine thermal history in the Oetztal-Merano area (Eastern Alps). Memorie di scienze geologiche 35, 319-325.

Exel, R., 1998. Lagerstättenkundliche und montanhistorische Erhebungen über den Bergbau in Südtirol (Provinz Bozen, Italien). Berichte der Geologischen Bundesanstalt 42, 131.

Favaro, S., Handy, M.R., Scharf, A., Schuster, R., 2017. Changing patterns of exhumation and denudation in front of an advancing crustal indenter, Tauern Window (Eastern Alps). Tectonics 36, 1053-1071.

Frisch, W., Dunkl, I., Kuhlemann, J., 2000. Post-collisional orogen-parallel large-scale extension in the Eastern Alps. Tectonophysics 327, 239-265.

Furlani, M., 1921. Studien über die Triaszonen im Hochpustertal, Eisack- und Pensertal in Tirol. Denkschriften der kaiserlichen Akademie der Wissenschaften mathematisch-naturwissenschlaftliche Klasse 97, 33-55.

Godard, G., Martin, S., Prosser, G., Kienast, J.R., Morten, L., 1996. Variscan migmatites, eclogites and garnet-peridotites of the Ulten zone, Eastern Austoalpine system. Tectonophysics 259, 313-341.

Griesmeier, G.E., Schuster, R., Grasemann, B., 2019. Major fault zones in the Austroalpine units of the Kreuzeck Mountains south of the Tauern Window (Eastern Alps, Austria). Swiss Journal of Geosciences 112, 39-53.

Habler, G., Thöni, M., Grasemann, B., 2009. Cretaceous metamorphism in the Austroalpine Matsch Unit (Eastern Alps): the interrelation between deformation and chemical equilibration processes. 97, 149.

Hammer, W., 1912. Blatt 5345 Glurns und Ortler (mit Erläuterungen), Geologische Spezialkarte der Österreichisch-Ungarischen Monarchie, k. k.

Heinisch, H., Schmidt, K., 1984. Zur Geologie des Thurntaler Quarzphyllits und des Altkristallins südlich des Tauernfensters (Ostalpen, Südtirol). Geologische Rundschau 73, 113-129.

Heinisch, H., Schmidt, K., Schuh, H., 1983. Zur geologischen Geschichte des Gailtalkristallins im unteren Lesachtal westlich von Kötschach-Mauthen (Kärnten, Österreich). Jahrbuch der Geologischen Bundesanstalt 126, 477-486.

Hoinkes, G., Koller, F., Rantitsch, G., Dachs, E., Höck, V., Neubauer, F., Schuster, R., 1999. Alpine metamorphism of the Eastern Alps. Schweizerische Mineralogische und Petrographische Mitteilungen 79, 155-181.

Holland, T., Powell, R., 1998. An internally consistent thermodynamic data set for phases of petrological interest. Journal of metamorphic Geology 16, 309-343.

Jäger, E., Niggli, E., 1967. Geological meaning of Rb-Sr age results as studied on samples from the Central Alps, Radioactive dating and methods of low-level counting. Proceedings of a symposium.

Klotz, T., Pomella, H., Reiser, M., Fügenschuh, B., Zattin, M., 2019. Differential uplift on the boundary between the Eastern and the Southern European Alps: Thermochronologic constraints from the Brenner Base Tunnel. Terra Nova 31, 281-294.

Knoll, T., Schuster, R., Huet, B., Mali, H., Onuk, P., Horschnegg, M., Ertl, A., Giester, G., 2018. Spodumen Pegmatites

and related Leucogranites from the Austroalpine unit (Eastern Alps, Central Europe): Field relations, Petrography, Geochemistra, and Geochronology. The Canadian Mineralogist 56, 1-40.

Konzett, J., Hoinkes, G., 1996. Paragonite-hornblende assemblages and their petrological significance: an example from the Austroalpine Schneeberg Complex, Southern Tyrol, Italy. Journal of Metamorphic Geology 14, 85-101.

Kunz, B.E., Manzotti, P., von Niederhäusern, B., Engi, M., Darling, J.R., Giuntoli, F., Lanari, P., 2018. Permian high-temperature metamorphism in the Western Alps (NW Italy). International Journal of Earth Sciences 107, 203-229.

Ludwig, K., 2008. Manual for Isoplot 3.7: Berkeley Geochronology Center Special Publication 4. California.

Luth, S., Willingshofer, E., ter Borgh, M., Sokoutis, D., Van Otterloo, J., Versteeg, A., 2013. Kinematic analysis and analogue modelling of the Passeier-and Jaufen faults: implications for crustal indentation in the Eastern Alps. International Journal of Earth Sciences 102, 1071-1090.

Luth, S.W., Willingshofer, E., 2008. Mapping of the post-collisional cooling history of the Eastern Alps. Swiss Journal of Geosciences 101, 207-223.

Mair, V., Nocker, C., Tropper, P., 2007. Das Ortler-Campo Kristallin in Südtriol. Mitt. Österr. Miner. Ges. 153.

Mair, V., Schuster, R., 2003. New geochronological data from the austroalpine Ortler crystalline in the Martell Valley (Südtirol, Italien). PG 46.

Martin, S., Montresor, L., Mair, V., Pellegrini, G.B., Avanzini, M., Fellin, G., Gambillara, R., Tumiati, S., Santuliana, E., Monopoli, B., Gaspari, D., Sapigni, M., Surian, N., 2009a. Erläuterungen zur geologischen Karte von Italien im Maßstab 1:50.000 Blatt 025 Rabbi. ISPRA, Istituto Superiore per la Protezione e la Ricerca Ambientale, Roma.

Martin, S., Montresor, L., Mair, V., Pellegrini, G.B., Avanzini, M., Fellin, G., Gambillara, R., Tumiati, S., Santuliana, E., Monopoli, B., Gaspari, D., Sapigni, M., Surian, N., 2009b. Note illustrative della Carta Geologica d'Italia - Rabbi foglio 026. Land Technology & Services - Treviso, Roma.

McArthur, J.M., Howarth, R.J., Bailey, T.R., 2001. Strontium Isotope Stratigraphy: LOWESS Version 3: Best Fit to the Marine Sr-Isotope Curve for 0-509 Ma and Accompanying Look-up Table for Deriving Numerical Age (Look-Up Table Version 4: 08/ 03). The Journal of Geology 109, 155-170.

Müller, W., Prosser, G., Mancktelow, N., Villa, I., Kelley, S., Viola, G., Oberli, F., Nemes, F., Neubauer, F., 2001. Geochronological constraints on the evolution of the Periadreatic Fault System (Alps). International Journal of Earth Sciences 90, 623-653.

Ortner, H., Reiter, F., Acs, P., 2002. Easy handling of tectonic data: the programs TectonicVB for Mac and TectonicsFP for Windows™. Computers & Geosciences 28, 1193-1200.

Pleuger, J., Mancktelow, N., Zwingmann, H., Manser, M., 2012. K–Ar dating of synkinematic clay gouges from Neoalpine faults of the Central, Western and Eastern Alps. Tectonophysics 550, 1-16.

Pomella, H., 2010. The Cenozoic evolution of the Giudicarie fault system (Eastern/Southern Alps, northern Italy). A geochronological, structural and paleomagnetic study, Institute of Geology and Paläontology. University of Innsbruck, p. 150.

Pomella, H., Flöss, D., Speckbacher, R., Tropper, P., Fügenschuh, B., 2016. The western end of the Eoalpine High-Pressure Belt (Texel unit, South Tyrol / Italy). Terra Nova 28, 60-69.

Pomella, H., Klötzli, U., Scholger, R., Stipp, M., Fügenschuh, B., 2011. The Northern Giudicarie and the Meran-Mauls fault (Alps, Northern Italy) in the light of new paleomagnetic and geochronological data from boudinaged Eo-/Oligocene tonalites. International Journal of Earth Sciences 100, 1827-1850.

Pomella, H., Stipp, M., Fügenschuh, B., 2012. Thermochronological record of thrusting and strike-slip faulting along the Giudicarie Fault System (Alps, Northern Italy). Tectonophysics 579, 118-130.

Potro, M.N., 1982. Petrographie, Metamorphose, Tektonik und Metallogenese im Mittleren Vinschgau/ Südtirol, N-Italien. Rheinisch-Westfälische Technische Hochschule, Aachen.

Prosser, G., 2000. The development of the North Giudicarie fault zone (Insubric line, Northern Italy). Journal of Geodynamics 30, 229-250.

Puhr, B., Schuster, R., Hoinkes, G., Moshammer, B., 2009. 87Sr/86Sr isotope study on marbles of the Austroalpine basement (Eastern Alps): tectonic implications and age constraints. 9th Workshop on Alpine Geological Studies, Cogne Abstract Volume.

Reiter, F., Acs, P., 1996-2000. TectonicsFP. Computer Software for Structural Geology, 2.0 ed.

Reiter, F., Freudenthaler, C., Hausmann, H., Ortner, H., Lenhardt, W., Brandner, R., 2018. Active seismotectonic deformation in front of the Dolomites indenter, Eastern Alps. Tectonics 37, 4625-4654.

Sander, B., 1906. Geologische Beschreibung des Brixner Granits. Jahrbuch der k. k. geologischen Reichsanstalt 56, 707-744.

Sander, B., 1929. Erläuterungen zur geologischen Karte Meran-Brixen. Der Schlern 16, 1-111.

Sander, B., Hammer, W., 1926. Note illustrative della Carta Geologica delle Tre Venezie - Foglio Merano. Società Cooperativa Tipografica, Padova.

Satir, M., 1975. Die Entwicklungsgeschichte der Westlichen Hohen Tauern und der südlichen Ötztalmasse auf Grund radiometrischer Altersbestimmungen. Mem. Ist. Geol. Min. Univ. Padova 30, 82.

Scharf, A., Handy, M.R., Favaro, S., Schmid, S.M., Bertrand, A., 2013. Modes of orogen-parallel stretching and extensional exhumation in response to microplate indentation and roll-back subduction (Tauern Window, Eastern Alps). International Journal of Earth Sciences, 1-28.

Schiavo, A., Dal Piaz, G.V., Monopoli, B., Bistacchi, A., Dal Piaz, G., Massironi, M., Toffolon, G., 2015. Geology of the Brenner pass-Fortezza transect, Italian eastern Alps. Journal of Maps 11, 201-215.

Schindelmayr, W.U., 1968. Geologische Untersuchungen in der Umgebung von Mauls und Stilfes in Südtirol. Ludwig Mayimilian Universität München.

Schmid, S.M., Fügenschuh, B., Kissling, E., Schuster, R., 2004. Tectonic map and overall architecture of the Alpine orogen. Eclogae Geologicae Helvetiae, Swiss Journal of Geosciences 97, 93-117.

Schneider, S., Hammerschmidt, K., Rosenberg, C.L., Gerdes, A., Frei, D., Bertrand, A., 2015. U–Pb ages of apatite in the western Tauern Window (Eastern Alps): Tracing the onset of collision-related exhumation in the European plate. Earth and Planetary Science Letters 418, 53-65.

Schulz, B., Steenken, A., Siegesmund, S., 2008. Geodynamic evolution of an Alpine terrane—the Austroalpine basement to the south of the Tauern window as a part of the Adriatic Plate (eastern Alps). Geological Society, London, Special Publications 298, 5-44.

Schuster, R., Koller, F., Höck, V., Hoinkes, G., Bousquet, R., 2004. Explanatory notes to the map: Metamorphic structure of the Alps: Metamorphic evolution of the Eastern Alps. Mitteilungen der Österreichischen Mineralogischen Gesellschaft, 175-199.

Schuster, R., Schabert, S., Abart, R., Frank, W., 2001. Permo-Triassic extension and related HT/LP metamorphism in the Austroalpine-Southalpine realm. Mitteilungen der Geologie und Bergbaustudenten Österreichs 44, 11-141.

Schuster, R., Stüwe, K., 2008. Permian metamorphic event in the Alps. Geology 36, 603-606.

Schuster, R., Tropper, P., Krenn, E., Finger, F., Frank, W., Philippitsch, R., 2015. Prograde Permo-Triassic metamorphic HT/LP assemblages from the Austroalpine Jenig Complex (Carinthia, Austria). Austrian Journal of Earth Sciences 108, 73-90.

Sölva, H., Grasemann, B., Thöni, M., Thiede, R., Habler, G., 2005. The Schneeberg Normal Fault Zone: Normal faulting associated with Cretaceous SE-directed extrusion in the Eastern Alps (Italy/Austria). Tectonophysics 401, 143-166.

Sölva, H., Thöni, M., Grasemann, B., Linner, M., 2001. Emplacement of eo-Alpine high-pressure rocks in the Austroalpine Ötztal complex. Geodinamica Acta 14, 345-360.

Sölva, H., Thöni, M., Habler, G., 2003. Dating a single garnet crystal with very high Sm/Nd ratios (Campo basement unit, Eastern Alps). European journal of mineralogy 15, 35-42.

Spiess, R., 1992. Petrographisch-geologische und geochronologische Untersuchungen zur Bildung der Mylonitzone am Westende des Penser-Joch-Zuges. Der Schlern 40, 95-104.

Spiess, R., 1995. The Passeier-Jaufen Line: a tectonic boundary between Variscan and eo-Alpine Meran-Mauls basement. Schweizerische Mineralogische und Petrographische Mitteilungen 75, 413-425.

Stipp, M., Stünitz, H., Heilbronner, R., Schmid, S.M., 2002. The eastern Tonale fault zone: a "natural laboratory" for crystal plastic deformation of quarz over a temperature range from 250 – 700°C. Journal of Structural Geology 24, 1861-1884.

Stöckhert, B., 1984. K-Ar determinations on muscovites and phengites from deformed pegmatites, and the minimum age of the old alpine deformation in the Austridic Basement to the south of the western Tauern Window (Ahrn valley, Southern Tyrol, Eastern Alps). Neues Jahrbuch für Mineralogie. Abhandlungen 150, 103-120.

Stöckhert, B., 1985. Pre-Alpine history of the Austridic basement to the south of the western Tauern Window (Southern Tyrol, Italy)-Caledonian versus Hercynian event. Neues Jahrbuch für Geologie und Paläontologie. Monatshefte 10, 618-642.

Thöni, M., 1981. Degree and evolution of the Alpine metamorphism in the Austroalpine Unit W of the Hohe Tauern in the light of K/Ar and Rb/Sr age determinations on micas. Jahrbuch der Geologischen Bundesanstalt 124, 111-174.

Thöni, M., 1983. The thermal climax of the early Alpine metamorphism in the Austroalpine thrust sheet. Memorie di scienze geologiche 36, 211-238.

Thöni, M., 1996. Isotopengeologie und Geochronologie–Einsatzmöglichkeiten in der Geologie. Mitteilungen der Geologie und Bergbaustudenten Österreichs 39, 187-209.

Thöni, M., Miller, C., 2009. The "Permian event" in the Eastern European Alps: Sm–Nd and P–T data recorded by multi-stage garnet from the Plankogel unit. Chemical Geology 260, 20-36.

Tropper, P., Hoinkes, G., 1996. Geothermobarometry of Al 2 SiO 5-bearing metapelites in the western Austroalpine Ötztal-basement. Mineralogy and Petrology 58, 145-170.

Tropper, P., Recheis, A., 2003. Garnet zoning as a window into the metamorphic evolution of a crystalline complex: the northern and central Austroalpine Ötztal-Complex as a polymorphic example. Mitteilungen der Österreichischen Geologischen Gesellschaft 94, 27-53.

Unterwurzacher, M., 2009. Tiroler Marmore als historische Werkstoffe - Vorkommen und Materialcharakterisierung. Archaeo Plus 1, 156-161.

Viola, G., Mancktelow, N., Seward, D., Meier, A., Martin, S., 2003. The Pejo fault system: An example of multiple tectonic activity in the Italian Eastern Alps. GSA Bulletin 115, 515-532.

Viola, G., Mancktelow, N.S., Seward, D., 2001. Late Oligocene-Neogene evolution of Europe-Adria collision: New structural and geochronological evidence from the Giudicarie fault system (Italian Eastern Alps). Tectonics 20, 999-1020.

Received: 6.10.2021
Accepted: 13.1.2022
Editorial Handling: Kurt Stüwe

Appendix

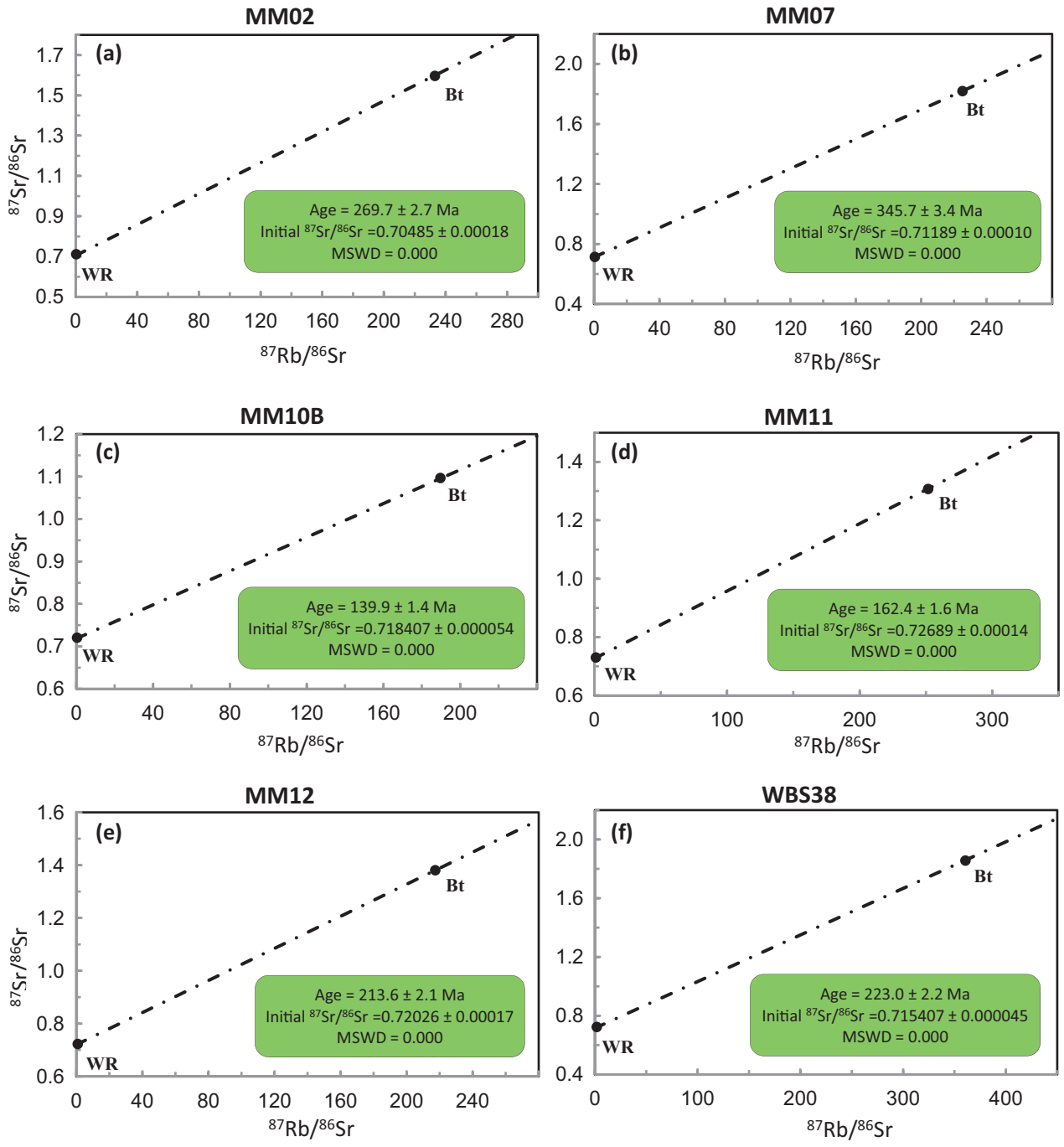

Figure A1: The graphs (a) to (f) show the calculated isochrones and Rb/Sr-ages on biotite of the MMNS. WR: Whole Rock; Bt: Biotit; MSWD: Mean square weighted deviation.

Sample	S 143	HM 314	S097	*LLD*
SiO_2	1.72	1.08	0.77	*0.01%*
Al_2O_3	0.62	0.15	0.13	*0.01%*
Fe_2O_3	0.48	0.62	0.02	*0.01%*
MnO	0.08	0.17	0.03	*0.01%*
MgO	0.85	0.99	0.35	*0.01%*
CaO	49.88	51.86	50.02	*0.01%*
Na_2O	< 0.01	< 0.01	< 0.01	*0.02%*
K_2O	0.18	< 0.01	< 0.01	*0.01%*
TiO_2	0.03	< 0.01	< 0.01	*0.01%*
P_2O_5	0.04	0.02	0.03	*0.01%*
L.O.I.	n.d.	n.d.	n.d.	*0.01%*
Total	53.88	54.89	52.24	- - - - -
Ba	250	< 10	1210	*10 ppm*
Cl	< 10	40	30	*10 ppm*
Rb	6	2	< 1	*1 ppm*
S	180	260	90	*10 ppm*
Sr	178	227	185	*1 ppm*

EDXRFA (Spectro-Xepos), calibration: SRMs - Lucas-Tooth-Modell, samples: glass discs and/or powder pellets. Major elements as oxide wt.%, Fe as Fe_2O_3tot., trace elements in ppm, L.O.I. at 1000°C/2h, analysis on dry basis (105°C/24h).
L.O.I. = loss on ignition, LLD = Lower Limit of Detection, n.d. = not determined

Table A1: Results of the XRF analyses on three samples taken from the marble belt within the Schenna unit.

Sample	E-UTM	N-UTM	Altitude	Lithology	Tectonic unit
A93	689943	5190054	1267	Quartz mylonite	Schenna unit
A94	690984	5190381	1318	Pegmatite	Schenna unit
A95	689999	5189984	1303	Paragneiss	Schenna unit
97c	675841	5178646	1876	Paragneiss	Schenna unit
HM314	674461	5177158	2255	Marble	Schenna unit
HM349	672945	5176245	1605	Marble	Schenna unit
MM02	674214	5181161	1752	Paragneiss	Hirzer unit
MM07	673566	5182267	1430	Orthogneis	St. Leonhard unit
MM10	669837	5175908	1037	Paragneis	Hirzer unit
MM11	672122	5174958	1589	Paragneis	Schenna unit
MM12	669975	5173582	1382	Paragneiss	Schenna unit
RBV12	673042	5176390	1779	Paragneiss	Schenna unit
S097	675828	5178745	1790	Marble	Schenna unit
S143	674440	5177221	2265	Marble	Schenna unit
WBS29	676567	5179260	1783	Marble	Schenna unit
WBS35	679530	5181478	1963	Marble	Schenna unit
WBS36	679530	5181478	1963	Marble	Schenna unit
WBS47	677606	5179980	2119	Marble	Schenna unit

Table A2: Sample list and geographic coordinates in UTM WGS84 32N.

Table A3: Representative electron-probe microanalysis of the silicate minerals.

Staurolite			**Biotite**			**Muscovite, Margarite**				**Garnet**			**Plagioclase**			**Chlorite**		
Sample	**RBV11**	**97c**	**Sample**	**97c**	**97c**	**Sample**	**RBV12**	**97c**	**RBV12**	**97c**	**Sample**	**97c**	**97c**	**Sample**	**97c**	**97c**	**Sample**	**RBV12**	**97c**
	Sta-1	**Sta-2**		**Bt-3**	**Bt-4**		**Ms-1**	**Ms-2**	**Mrg-1**	**Mrg-1**		**Grt-2**	**Grt-5**		**Pl-1**	**Pl-2**		**Chl-1**	**Chl-1**
P_2O_5	0.01	n.d.	P_2O_5	n.d.	n.d.	P_2O_5	0.00	n.d.	0.01	n.d.				P_2O_5	n.d.	n.d.	P_2O_5	0.02	n.d.
SiO_2	28.57	27.90	SiO_2	35.78	36.01	SiO_2	46.22	46.58	35.15	35.13	SiO_2	37.84	37.70	SiO_2	59.69	65.67	SiO_2	22.72	22.67
TiO_2	0.52	0.76	TiO_2	2.61	2.13	TiO_2	0.14	0.74	0.05	0.20	TiO_2	0.02	0.06	TiO_2	n.d.	n.d.	TiO_2	n.d.	0.08
Al_2O_3	55.53	55.19	Al_2O_3	18.77	19.08	Al_2O_3	37.08	35.37	47.42	45.36	Al_2O_3	21.36	21.51	Al_2O_3	25.26	20.77	Al_2O_3	26.07	29.10
Cr_2O_3	0.05	n.d.	Cr_2O_3	n.d.	n.d.	Fe_2O_3	n.c.	n.c.	n.c.	n.c.	Fe_2O_3	n.c.	n.c.	Cr_2O_3	n.d.	n.d.	Cr_2O_3	0.02	n.d.
Fe_2O_3	n.c.	n.c.	Fe_2O_3	n.c.	n.c.	FeO	1.87	0.97	0.68	1.49	FeO	31.65	31.09	Fe_2O_3	n.c.	n.c.	Fe_2O_3	n.c.	n.c.
FeO	11.87	8.79	FeO	19.27	17.62	MnO	0.05	0.06	0.04	0.07	MnO	4.89	5.10	FeO	0.09	n.d.	FeO	30.25	23.87
MnO	0.19	0.34	MnO	0.12	0.07	MgO	0.41	0.59	0.09	0.27	MgO	2.34	2.12	MnO	0.05	0.04	MnO	0.15	0.29
MgO	0.79	0.98	MgO	8.41	9.58	CaO	n.d.	n.d.	8.14	7.04	CaO	2.11	1.97	MgO	n.d.	n.d.	MgO	8.32	9.75
CaO	n.d.	n.d.	CaO	n.d.	0.01	ZnO	0.07	0.12	0.06	0.61	ZnO	n.d.	0.07	CaO	7.16	1.99	CaO	0.02	0.14
ZnO	0.12	4.03	ZnO	n.d.	0.19	Na_2O	0.48	1.04	1.84	1.68	Na_2O	0.03	0.03	ZnO	0.07	0.08	ZnO	0.02	0.54
Na_2O	n.d.	0.04	Na_2O	0.10	0.16	K_2O	10.26	9.89	1.27	2.06	K_2O	0.10	0.22	Na_2O	7.79	10.35	Na_2O	0.04	0.04
K_2O	0.02	0.02	K_2O	9.75	9.36	Cl	n.d.	0.01	n.d.	0.03	Cl	0.01	n.d.	K_2O	0.05	0.10	K_2O	0.01	0.23
Cl			Cl	0.01	0.00									Cl	n.d.	n.d.	Cl	n.d.	0.03
Σoxides	97.67	98.05	Σoxides	94.82	94.21	Σoxides	96.59	95.37	94.78	93.94	Σoxides	100.34	99.86	Σoxides	100.16	99.01	Σoxides	87.63	86.74
P	0.002	n.d.	P	n.d.	n.d.	P	n.d.	n.d.	n.d.	n.d.				P	n.d.	n.d.	P	0.001	n.d.
Si	7.843	7.701	Si	2.738	2.745	Si	3.036	3.087	2.325	2.365	Si	3.028	3.029	Si	2.661	2.913	Si	1.931	1.884
Ti	0.108	0.158	Ti	0.150	0.122	Ti	0.007	0.037	0.003	0.010	Ti	0.001	0.004	Ti	n.d.	n.d.	Ti	n.d.	0.005
Al	17.970	17.955	Al	1.693	1.714	Al	2.869	2.764	3.696	3.600	Al	2.015	2.038	Al	1.327	1.085	Al	2.611	2.850
Cr	0.012	n.d.	Cr	n.d.	n.d.	Cr	0.001	n.d.	0.002	n.d.				Cr	n.d.	n.d.	Cr	0.001	n.d.
Fe^{3+}	n.c.	n.c.	Fe^{3+}	n.c.	n.c.	Fe^{3+}	n.c.	n.c.	n.c.	n.c.	Fe^{3+}	n.c.	n.c.	Fe^{3+}	n.c.	n.c.	Fe^{3+}	n.c.	n.c.
Fe^{2+}	2.729	2.028	Fe^{2+}	1.233	1.123	Fe^{2+}	0.103	0.054	0.038	0.083	Fe^{2+}	2.118	2.090	Fe^{2+}	0.003	n.d.	Fe^{2+}	2.149	1.659
Mn	0.045	0.080	Mn	0.008	0.005	Mn	0.003	0.004	0.002	0.004	Mn	0.332	0.347	Mn	0.002	0.002	Mn	0.011	0.020
Mg	0.325	0.404	Mg	0.959	1.088	Mg	0.040	0.058	0.008	0.027	Mg	0.280	0.254	Mg	n.d.	n.d.	Mg	1.052	1.207
Ca	n.d.	n.d.	Ca	n.d.	n.d.	Ca	n.d.	n.d.	0.578	0.508	Ca	0.181	0.170	Ca	0.342	0.095	Ca	0.002	0.012
Zn	0.023	0.820	Zn	n.d.	0.010	Zn	0.003	0.006	0.003	0.031	Zn	0.000	0.004	Zn	0.002	0.003	Zn	0.001	0.033
Na	n.d.	0.020	Na	0.014	0.024	Na	0.062	0.134	0.237	0.219	Na	0.004	0.005	Na	0.673	0.889	Na	0.006	0.006
K	0.007	0.007	K	0.952	0.910	K	0.860	0.836	0.106	0.177	K	0.010	0.022	K	0.003	0.006	K	0.001	0.024
			Cl	0.002	0.002	Cl	n.d.	0.001	n.d.	0.003	Cl	0.001	n.d.	Cl	n.d.	n.d.	Cl	n.d.	0.004
X_{Fe}	0.89	0.83	X_{Mg}	0.44	0.49	X_K	0.93	0.86	0.12	0.20	Almandin	0.73	0.73	X_{Na}	0.66	0.90	X_{Na}	n.d.	n.d.
			Ti apfu	0.30	0.24	X_{Ca}	0.00	0.00	0.63	0.56	Spessartin	0.11	0.12	X_{Ca}	0.34	0.09	X_{Ca}	n.d.	n.d.
						X_{Na}	0.07	0.14	0.25	0.24	Pyrop	0.10	0.09	X_K	n.d.	0.01	X_K	n.d.	n.d.
											Grossular	0.06	0.06	X_{Mg}	n.d.	n.d.	X_{Mg}	0.33	0.42
Σcations	29.064	29.173	Σcations	7.75	7.74	Σcations	6.98	6.98	7.00	7.03	Σcations	7.970	7.963	Σcations	5.01	4.99	Σcations	7.77	7.71

The analysis are given in in weight% oxides. The basis of formula calculations are as follows: Staurolite 46 O and 30 cations + OH; Biotite 11 O and 8 cations; Muscovite 11 O and 7 cations; Garnet: 12 O 8 cations; Plagioclase: 8 O and 5 cations; Chlorite 14 O + OH.

n.d. = not deteced n.c. = not calculated apfu = atoms per formula unit

Sample	WBS29 Cal01:r	WBS29 Cal02:c	WBS29 Cal03:r	WBS35 Cal04:r	WBS35 Cal05:r	WBS35 Cal06:r	WBS35 Cal06:c	WBS35 Cal07:r	WBS35 Cal08:r	WBS35 Cal11:c	WBS35 Cal12:r	WBS35 Cal13:c	WBS36 Cal09:r	WBS36 Cal10:r	WBS36 Cal22:r	WBS36 Cal25:r	S097 Cal01:r	S097 Cal03:r
SiO_2	n.d.	n.d.	n.d.	n.d.	n.d.	n.d.	1.02	n.d.	n.d.	0.03	n.d.	n.d.	n.d.	n.d.	0.05	0.02	n.d.	n.d.
TiO_2	n.d.	n.d.	n.d.	n.d.	n.d.	n.d.	0.03	n.d.	n.d.	n.d.	n.d.	n.d.	n.d.	n.d.	0.01	0.03	n.d.	n.d.
Al_2O_3	n.d.	n.d.	n.d.	n.d.	n.d.	n.d.	n.d.	n.d.	n.d.	n.d.	n.d.	n.d.	n.d.	n.d.	n.d.	n.d.	n.d.	n.d.
Cr_2O_3	n.d.	n.d.	n.d.	n.d.	n.d.	n.d.	0.03	n.d.	n.d.	n.d.	n.d.	n.d.	n.d.	n.d.	n.d.	0.01	n.d.	n.d.
Fe_2O_3	n.e.	n.e.	n.e.	n.e.	n.e.	n.e.	n.e.	n.e.	n.e.	n.e.	n.e.	n.e.	n.e.	n.e.	n.e.	n.e.	n.e.	n.e.
FeO	n.d.	n.d.	0.10	0.84	0.95	0.44	0.35	0.61	0.61	0.83	0.69	0.99	0.17	0.18	0.13	0.23	0.40	0.60
MnO	0.49	0.43	0.39	0.66	0.74	0.67	0.53	0.67	0.73	0.94	0.74	0.78	0.31	0.36	0.35	0.62	0.20	0.05
MgO	0.58	0.37	0.46	2.02	2.21	0.67	0.79	0.85	0.98	1.51	1.21	2.61	1.15	0.97	0.98	0.84	0.77	0.65
CaO	54.45	55.52	54.40	51.97	51.75	53.47	56.72	53.55	53.19	55.14	51.61	50.02	52.99	53.42	55.43	56.32	56.36	55.96
Na_2O	n.d.	n.d.	n.d.	n.d.	n.d.	n.d.	0.04	n.d.	n.d.	0.01	n.d.	n.d.	n.d.	n.d.	0.02	n.d.	n.d.	n.d.
K_2O	n.d.	n.d.	n.d.	n.d.	n.d.	n.d.	n.d.	n.d.	n.d.	n.d.	n.d.	n.d.	n.d.	n.d.	n.d.	n.d.	n.d.	n.d.
ΣOxide	55.51	56.32	55.34	55.48	55.65	55.26	59.51	55.68	55.51	58.47	54.25	54.40	54.62	54.92	56.96	58.07	57.73	57.26
Si	n.d.	n.d.	n.d.	n.d.	n.d.	n.d.	0.016	n.d.	n.d.	0.001	n.d.	n.d.	n.d.	n.d.	0.001	n.d.	n.d.	n.d.
Ti	n.d.	n.d.	n.d.	n.d.	n.d.	n.d.	n.d.	n.d.	n.d.	n.d.	n.d.	n.d.	n.d.	n.d.	n.d.	n.d.	n.d.	n.d.
Al	n.d.	n.d.	n.d.	n.d.	n.d.	n.d.	n.d.	n.d.	n.d.	n.d.	n.d.	n.d.	n.d.	n.d.	n.d.	n.d.	n.d.	n.d.
Cr	n.d.	n.d.	n.d.	n.d.	n.d.	n.d.	n.d.	n.d.	n.d.	n.d.	n.d.	n.d.	n.d.	n.d.	n.d.	n.d.	n.d.	n.d.
Fe^{3+}	n.e.	n.e.	n.e.	n.e.	n.e.	n.e.	n.e.	n.e.	n.e.	n.e.	n.e.	n.e.	n.e.	n.e.	n.e.	n.e.	n.e.	n.e.
Fe^{2+}	n.d.	n.d.	0.001	0.012	0.013	0.006	0.004	0.009	0.009	0.011	0.010	0.014	0.002	0.003	0.002	0.003	0.005	0.008
Mn	0.007	0.006	0.006	0.009	0.010	0.010	0.007	0.010	0.010	0.013	0.011	0.011	0.005	0.005	0.005	0.008	0.003	0.001
Mg	0.014	0.009	0.011	0.050	0.055	0.017	0.018	0.021	0.025	0.036	0.031	0.066	0.029	0.024	0.024	0.020	0.019	0.016
Ca	0.979	0.985	0.982	0.929	0.921	0.967	0.937	0.961	0.956	0.939	0.948	0.909	0.964	0.968	0.968	0.967	0.973	0.975
Na	n.d.	n.d.	n.d.	n.d.	n.d.	n.d.	0.001	n.d.	n.d.	n.d.	n.d.	n.d.	n.d.	n.d.	0.001	n.d.	n.d.	n.d.
K	n.d.	n.d.	n.d.	n.d.	n.d.	n.d.	n.d.	n.d.	n.d.	n.d.	n.d.	n.d.	n.d.	n.d.	n.d.	n.d.	n.d.	n.d.
X_{Ca}	0.98	0.98	0.98	0.93	0.92	0.97	0.97	0.96	0.96	0.94	0.95	0.91	0.96	0.97	0.97	0.97	0.97	0.98
X_{Mg}	0.01	0.01	0.01	0.05	0.06	0.02	0.02	0.02	0.02	0.04	0.03	0.07	0.03	0.02	0.02	0.02	0.02	0.02
X_{Fe}	n.d.	n.d.	n.d.	0.01	0.01	0.01	n.d.	0.01	0.01	0.01	0.01	0.01	n.d.	n.d.	n.d.	n.d.	0.01	0.01
X_{Mn}	0.01	0.01	0.01	0.01	0.01	0.01	0.01	0.01	0.01	0.01	0.01	0.01	n.d.	0.01	n.d.	0.01	n.d.	n.d.

Basis of formula calculation for calcite: 1 O n.d. = not detected n.e. = not examined r = rim c = core

Sample	WBS29 Dol21:r	WBS29 Dol1:r	WBS35 Dol2:r	WBS35 Dol3:c	WBS35 Dol10:r	WBS36 Dol3:c	WBS36 Dol4:c	WBS36 Dol19:c	WBS36 Dol20:r	S097 Dol1:c
SiO_2	0.02	n.d.	n.d.	0.08	0.04	n.d.	n.d.	0.03	0.03	n.d.
TiO_2	n.d.	n.d.	n.d.	n.d.	0.01	n.d.	n.d.	0.02	n.d.	n.d.
Al_2O_3	n.d.	n.d.	n.d.	0.01	0.00	n.d.	n.d.	n.d.	n.d.	n.d.
Cr_2O_3	0.01	n.d.	n.d.	0.01	0.04	n.d.	n.d.	n.d.	0.01	n.d.
Fe_2O_3	n.e.	n.e.	n.e.	n.e.	n.e.	n.e.	n.e.	n.e.	n.e.	n.e.
FeO	0.80	2.82	3.00	2.85	3.20	0.09	1.54	1.18	0.24	3.57
MnO	0.39	0.57	0.90	0.75	1.04	0.29	0.31	0.39	0.23	0.35
MgO	21.22	19.67	19.73	19.44	19.04	21.58	20.54	20.30	21.50	18.97
CaO	29.44	29.76	29.56	29.33	28.90	30.30	29.46	29.33	29.80	30.10
Na_2O	0.01	n.d.	n.d.	n.d.	0.03	n.d.	n.d.	0.01	n.d.	n.d.
K_2O	0.01	n.d.	n.d.	n.d.	0.01	n.d.	n.d.	n.d.	n.d.	n.d.
ΣOxide	51.90	52.82	53.19	52.47	52.31	52.26	51.85	51.26	51.80	52.99
Si	0.001	n.d.	n.d.	0.003	0.001	n.d.	n.d.	0.001	0.001	n.d.
Ti	n.d.	n.d.	n.d.	n.d.	0.000	n.d.	n.d.	0.001	n.d.	n.d.
Al	n.d.	n.d.	n.d.	n.d.	0.000	n.d.	n.d.	n.d.	n.d.	n.d.
Cr	n.d.	n.d.	n.d.	n.d.	0.001	n.d.	n.d.	n.d.	n.d.	n.d.
Fe^{3+}	n.e.	n.e.	n.e.	n.e.	n.e.	n.e.	n.e.	n.e.	n.e.	n.e.
Fe^{2+}	0.021	0.074	0.078	0.075	0.085	0.002	0.040	0.031	0.006	0.094
Mn	0.010	0.015	0.024	0.020	0.028	0.007	0.008	0.010	0.006	0.009
Mg	0.985	0.916	0.914	0.911	0.900	0.990	0.960	0.959	0.995	0.886
Ca	0.982	0.996	0.984	0.988	0.982	1.000	0.990	0.996	0.991	1.011
Na	n.d.	n.d.	n.d.	n.d.	0.002	n.d.	n.d.	n.d.	n.d.	n.d.
K	n.d.	n.d.	n.d.	n.d.	n.d.	n.d.	n.d.	n.d.	n.d.	n.d.
X_{Ca}	0.49	0.50	0.49	0.50	0.49	0.50	0.50	0.50	0.50	0.51
X_{Mg}	0.49	0.46	0.46	0.46	0.45	0.50	0.48	0.48	0.50	0.44
X_{Fe}	0.01	0.04	0.04	0.04	0.04	n.d.	0.02	0.02	n.d.	0.05
X_{Mn}	0.01	0.01	0.01	0.01	0.01	n.d.	n.d.	0.01	n.d.	0.00

Basis of formula calculation for Dollomite: 2 O n.d. = not detected n.e. = not examined r = rim c = core

Table A4: Representative electron-probe microanalysis of the carbonates.

Sample S097

	cc-1	dol-1	cc-2	dol-1	cc-3	dol-1
Fe apfu	0.01	0.09	0.01	0.09	0.01	0.09
Mn apfu	0	0.01	0	0.01	0	0.01
Mg apfu	0.02	0.89	0.02	0.89	0.02	0.89
Ca apfu	0.97	1.01	0.97	1.01	0.98	1.01
Anovitz & Essene (1987)						
T(C)=	334		324		298	

Sample WBS29

	cc-1	dol-1	cc-2	dol-1	cc-3	dol-1
Fe apfu	0	0.09	0	0.09	0.01	0.09
Mn apfu	0.01	0.01	0.01	0.01	0	0.01
Mg apfu	0.01	0.89	0.01	0.89	0.02	0.89
Ca apfu	0.98	1.01	0.99	1.01	0.98	1.01
Anovitz & Essene (1987)						
T(C)=	276		131		298	

Sample WBS36

	cc-9	dol-3	cc-10	dol-1	cc-11	dol-1
Fe apfu	0	0.04	0	0.09	0	0.09
Mn apfu	0	0.01	0.01	0.01	0.01	0.01
Mg apfu	0.03	0.46	0.02	0.89	0.03	0.89
Ca apfu	0.96	0.49	0.97	1.01	0.97	1.01
Anovitz & Essene (1987)						
T(C)=	424		390		408	

Sample Nr.WBS35

	cc-4	dol-2	cc-5	dol-1	cc-6	dol-1
Fe apfu	0.01	0.04	0.01	0.09	0.01	0.09
Mn apfu	0.01	0.01	0.01	0.01	0.01	0.01
Mg apfu	0.05	0.46	0.06	0.89	0.02	0.89
Ca apfu	0.93	0.49	0.92	1.01	0.97	1.01
Anovitz & Essene (1987)						
T(C)=	527		546		315	

Sample WBS35

	cc-7	dol-2	cc-8	dol-1	cc-12	dol-1
Fe apfu	0.01	0.04	0.01	0.09	0.01	0.09
Mn apfu	0.01	0.01	0.01	0.01	0.01	0.01
Mg apfu	0.05	0.46	0.02	0.89	0.03	0.89
Ca apfu	0.93	0.49	0.96	1.01	0.95	1.01
Anovitz & Essene (1987)						
T(C)=	527		391		436	

Sample WBS35

	cc-13	dol-2	cc-8	dol-1	cc-12	dol-1
Fe apfu	0.01	0.04	0.01	0.09	0.01	0.09
Mn apfu	0.01	0.01	0.01	0.01	0.01	0.01
Mg apfu	0.07	0.46	0.02	0.89	0.03	0.89
Ca apfu	0.91	0.49	0.96	1.01	0.95	1.01
Anovitz & Essene (1987)						
T(C)=	584		391		436	

cc = Calcite dol = Dolomite apfu = atoms per formula unit

Table A5: Results of Calcite-Dolomite geothermometry. apfu = atoms per formula unit